

This is an Open Access document downloaded from ORCA, Cardiff University's institutional repository: <https://orca.cardiff.ac.uk/id/eprint/175495/>

This is the author's version of a work that was submitted to / accepted for publication.

Citation for final published version:

Chen, Yuhang, Chen, Yongping, Xu, Zhenshan, Lin, Pengzhi and Xie, Zhihua 2025. Coupling of non-hydrostatic model with unresolved point-particle model for simulating particle-laden free surface flows. *Applied Mathematical Modelling* , 115962. 10.1016/j.apm.2025.115962

Publishers page: <http://dx.doi.org/10.1016/j.apm.2025.115962>

Please note:

Changes made as a result of publishing processes such as copy-editing, formatting and page numbers may not be reflected in this version. For the definitive version of this publication, please refer to the published source. You are advised to consult the publisher's version if you wish to cite this paper.

This version is being made available in accordance with publisher policies. See <http://orca.cf.ac.uk/policies.html> for usage policies. Copyright and moral rights for publications made available in ORCA are retained by the copyright holders.



Journal Pre-proof

Coupling of non-hydrostatic model with unresolved point-particle model for simulating particle-laden free surface flows

Yuhang Chen, Yongping Chen, Zhenshan Xu, Pengzhi Lin and Zhihua Xie

PII: S0307-904X(25)00037-X
DOI: <https://doi.org/10.1016/j.apm.2025.115962>
Reference: APM 115962

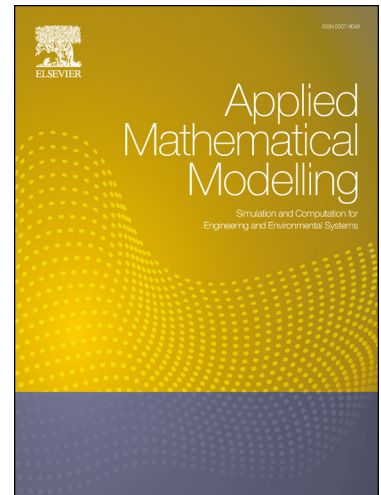
To appear in: *Applied Mathematical Modelling*

Received date: 9 May 2024
Revised date: 9 January 2025
Accepted date: 20 January 2025

Please cite this article as: Y. Chen, Y. Chen, Z. Xu et al., Coupling of non-hydrostatic model with unresolved point-particle model for simulating particle-laden free surface flows, *Applied Mathematical Modelling*, 115962, doi: <https://doi.org/10.1016/j.apm.2025.115962>.

This is a PDF file of an article that has undergone enhancements after acceptance, such as the addition of a cover page and metadata, and formatting for readability, but it is not yet the definitive version of record. This version will undergo additional copyediting, typesetting and review before it is published in its final form, but we are providing this version to give early visibility of the article. Please note that, during the production process, errors may be discovered which could affect the content, and all legal disclaimers that apply to the journal pertain.

© 2025 Published by Elsevier.



Highlights

- A two-phase flow model couples a non-hydrostatic model with a point-particle method.
- Free surface tracked using a Lagrangian-Eulerian method.
- Basset force's role in particle settling explored under various environments.
- The model is validated through benchmark cases of flow and particle transport.
- Simulations of sediment-laden jets in initially stationary water and flow with waves are presented.

14 Coupling of non-hydrostatic model with unresolved
15 point-particle model for simulating particle-laden free
16 surface flows

17 Yuhang Chen^{a,b,c}, Yongping Chen^{a,b,*}, Zhenshan Xu^{a,b}, Pengzhi Lin^d,
18 Zhihua Xie^{c,*}

^a*The National Key Laboratory of Water Disaster Prevention, Hohai
University, Nanjing, 210098, Jiangsu, China*

^b*College of Harbor, Coastal and Offshore Engineering, Hohai
University, Nanjing, 210098, Jiangsu, China*

^c*School of Engineering, Cardiff University, Queen's Buildings, Cardiff, CF24 3AA, UK*

^d*State Key Laboratory of Hydraulics and Mountain River Engineering, Sichuan
University, Chengdu, 610065, Sichuan, China*

19 **Abstract**

Sediment-laden flow is a common phenomenon in nature and the deposition of sediments can make a great difference in landscape formation or marine systems. The complexity of this issue can be further increased with temporal variations in the free surface elevation. This paper aims to present a two-phase flow model that effectively integrates the non-hydrostatic free surface model with the Lagrangian point-particle model. The free surface elevation is conceptualized as a height function and is tracked using a Lagrangian-Eulerian method. This new model is validated by five test cases, showing a good agreement with analytical or experimental results. This demonstrates the model's proficiency in handling sediment-laden flow under various free surface flow conditions, particularly with surface waves. Consequently, the proposed model holds promise for investigating sediment-laden flow issues in coastal regions.

20 *Keywords:* non-hydrostatic model, point-particle, particle-laden free
21 surface flows

*Corresponding authors.

Email address: ypchen@hhu.edu.cn (Yongping Chen); zxie@cardiff.ac.uk (Zhihua Xie)

22 1. Introduction

23 Sediment-laden free surface flow is a prevalent phenomenon in nature.
24 It is vital for comprehending a range of environmental and geological pro-
25 cesses. This interaction, characterized by the movement of water containing
26 sediment particles, significantly influences landscape formation [1, 2], river
27 [3, 4] and marine ecosystems [5, 6]. Understanding the intricate dynamics
28 in sediment-laden flow is essential for both appreciating natural mechanisms
29 and devising practical applications in the fields of environmental engineering
30 and hydrodynamics.

31 To effectively capture such phenomena, numerical simulation has emerged
32 as an efficient method. Over the past decade, extensive research has been con-
33 ducted on sediment transport patterns and various numerical models have
34 been utilized. They can be divided mainly into three categories, namely
35 Euler–Euler model [7–12], Euler–Lagrange model [13–16] and Lagrange–Lagrange
36 model [17–22]. The Euler–Euler model treats sediment phase as a continuum
37 and sediment transport is modeled using an advection–diffusion equation.
38 It effectively captures the sediment transport process by solving the mass
39 and momentum equations for both fluid and sediment phases, incorporating
40 closures for interphase momentum transfer, turbulence, and intergranular
41 stresses. However, for polydisperse particles or those particles with greater
42 inertia (Stokes (St) number ≥ 1), such kind of model encounters challenges
43 [23]. In such circumstances, the Lagrangian approach, where sediment parti-
44 cles are individually tracked via the Maxey–Riley equations [24], offers a more
45 suitable alternative. Apart from the Lagrange–Lagrange model, which treats
46 both fluid and sediment phases as particles, the Euler–Lagrange model can
47 achieve relatively good results with reasonable computational cost. Hence,
48 the Euler–Lagrange model is becoming more and more popular in simulating
49 two-phase flow problems.

50 The Euler–Lagrange model can be categorized into two main approaches:
51 the fully resolved particle model and the unresolved point-particle approach.
52 As for the fully resolved particle model, the immersed boundary method
53 [25–27] is adopted and no-slip boundary condition is directly enforced on
54 the surfaces of individual particles [28], necessitating a grid size smaller than
55 the sediment diameters to resolve both the particles and the detailed flow
56 fields around them. In that case, the fully resolved particle model has the
57 potential to substantially enhance our understanding of microscale sediment
58 transport processes and foster the development of improved closures for aver-

59 aged equations [29]. However, the limitations on the computational resources
60 are always a problem for simulating sediment transport at different spatial
61 and temporal scales [23]. By contrast, in the unresolved point-particle model,
62 particles are treated as point sources without resolving the particle–fluid in-
63 terfaces by the continuous phase grid, allowing for a grid size significantly
64 larger than the sediment diameter. Hence, the grid size in this model can
65 be several times larger than the sediment diameter. Considering its much
66 smaller computational cost, this approach is now well established as a re-
67 search tool in a number of fields [30–33], which is more suitable for applica-
68 tion when a large number of small particles are involved [34].

69 When simulating sediment-laden flows with free surface elevation changes
70 using the Euler–Lagrange model, the volume-of-fluid (VOF) method [35] is
71 commonly used and has been successfully applied in many conditions [36–
72 39]. This interface capturing method can capture the water surface well
73 although it is constrained by substantial computational demands. In con-
74 trast, non-hydrostatic models, which conceptualize the free-surface elevation
75 as a single-valued function dependent on horizontal coordinates, offer an ef-
76 ficient solution for tracking surface movements with reduced computational
77 demands [40]. The key advantage of non-hydrostatic models lies in their
78 ability to accurately predict wave dispersion with relatively few vertical grid
79 points. For example, studies by Lin and Li [41] and Ma et al. [42] have
80 shown that 10–20 vertical layers are sufficient to describe wave dispersion
81 to an acceptable level, even with simplified pressure boundary conditions at
82 the top layer. Further advancements [43, 44] enable even more computa-
83 tional efficiency by positioning pressure at the cell faces rather than at the
84 cell centers. Hence, these non-hydrostatic models have been widely used for
85 simulating free-surface flows in both ocean and coastal environments [41–49].
86 Ma et al. [50] used the non-hydrostatic model - NHWAVE to simulate both
87 turbidity currents and the tsunami wave generation by a landslide. Berard et
88 al. [51] simulated the bathymetry change of a steep sand dune under waves
89 using the XBeach model. Zhang et al. [52] proposed a two-layer coupled
90 model to investigate submarine landslides and resulting tsunami generation
91 over irregular bathymetry. However, in these models, the sediment phase is
92 considered as a continuum and in fact, they are all Euler-Euler models.

93 It can be seen from the above literature review that contemporary Euler–
94 Lagrange models predominantly utilize a combination of the Navier-Stokes
95 equation and an interface capturing method when applied to sediment-laden
96 flow problems with free surfaces. However, these models generally incur

97 higher computational costs than non-hydrostatic models. Most non-hydrostatic
 98 models are based on the Euler-Euler method when simulating particle-laden
 99 flows. The integration of non-hydrostatic models with the point-particle
 100 model remains relatively rare. It is evident that the fusion of non-hydrostatic
 101 models with point-particle models holds significant potential. This approach
 102 capitalizes on the relatively lower computational demands of non-hydrostatic
 103 models while enhancing the accuracy of transport patterns for particles with
 104 greater inertia, as facilitated by the point-particle model.

105 In this paper, the main novelty is to develop a two-phase flow model
 106 which couples the non-hydrostatic free surface model with a Lagrangian
 107 point-particle model to simulate dilute sediment-laden free surface flow prob-
 108 lems. A series of numerical simulation cases, encompassing regular waves,
 109 wave-structure interactions, a single spherical particle settling in stationary
 110 and oscillation environment, and sediment-laden jet in stationary and wave
 111 environments are conducted to verify the model's applicability. The paper is
 112 organized as follows: the governing equation and boundary conditions for the
 113 two-phase flow model are introduced in Section 2. The numerical methods
 114 are presented in Section 3. Five test cases are validated in Section 4. Finally,
 115 the conclusions are given in Section 5.

116 2. Governing equations

117 2.1. Continuous phase

118 A three-dimensional large eddy simulation model developed by Chen et
 119 al. [46] was adopted. The governing equations of fluid phase in the non-
 120 hydrostatic model are the spatially filtered Navier-Stokes equations, which
 121 can be written as:

$$\frac{\partial u_1}{\partial x^*} + \frac{\partial u_2}{\partial y^*} + \frac{\partial u_3}{\partial z^*} = 0 \quad (1)$$

$$\begin{aligned} \frac{\partial u_1}{\partial t^*} + u_1 \frac{\partial u_1}{\partial x^*} + u_2 \frac{\partial u_1}{\partial y^*} + u_3 \frac{\partial u_1}{\partial z^*} = & -\frac{1}{\rho_f} \frac{\partial p}{\partial x^*} + g_x + \frac{\partial \tau_{xx}}{\partial x^*} + \frac{\partial \tau_{xy}}{\partial y^*} + \frac{\partial \tau_{xz}}{\partial z^*} - \\ & \frac{\partial \tau_{xx}^{SGS}}{\partial x^*} - \frac{\partial \tau_{xy}^{SGS}}{\partial y^*} - \frac{\partial \tau_{xz}^{SGS}}{\partial z^*} \end{aligned} \quad (2)$$

$$\frac{\partial u_2}{\partial t^*} + u_1 \frac{\partial u_2}{\partial x^*} + u_2 \frac{\partial u_2}{\partial y^*} + u_3 \frac{\partial u_2}{\partial z^*} = -\frac{1}{\rho_f} \frac{\partial p}{\partial y^*} + g_y + \frac{\partial \tau_{yx}}{\partial x^*} + \frac{\partial \tau_{yy}}{\partial y^*} + \frac{\partial \tau_{yz}}{\partial z^*} - \frac{\partial \tau_{yx}^{SGS}}{\partial x^*} - \frac{\partial \tau_{yy}^{SGS}}{\partial y^*} - \frac{\partial \tau_{yz}^{SGS}}{\partial z^*} \quad (3)$$

$$\frac{\partial u_3}{\partial t^*} + u_1 \frac{\partial u_3}{\partial x^*} + u_2 \frac{\partial u_3}{\partial y^*} + u_3 \frac{\partial u_3}{\partial z^*} = -\frac{1}{\rho_f} \frac{\partial p}{\partial z^*} + g_z + \frac{\partial \tau_{zx}}{\partial x^*} + \frac{\partial \tau_{zy}}{\partial y^*} + \frac{\partial \tau_{zz}}{\partial z^*} - \frac{\partial \tau_{zx}^{SGS}}{\partial x^*} - \frac{\partial \tau_{zy}^{SGS}}{\partial y^*} - \frac{\partial \tau_{zz}^{SGS}}{\partial z^*} \quad (4)$$

122 where u_i ($i = 1, 2, 3$) are the velocity components in horizontal, transverse
 123 and vertical directions, respectively; (x^*, y^*, z^*, t^*) are the spatial and time
 124 coordinates in the physical domain; t is the time; p is the pressure; ρ_f is the
 125 water density; g_i ($i = 1, 2, 3$ or x, y, z) are the acceleration due to gravity; τ_{ij}
 126 and τ_{ij}^{SGS} ($i, j = 1, 2, 3$ or x, y, z) are shear stress and sub-grid scale (SGS)
 127 stress.

128 This model employs the σ coordinate in the vertical direction, as is shown
 129 below:

$$t = t^*, x = x^*, y = y^*, \sigma = \frac{z^* + h}{\eta + h} \quad (5)$$

130 where (x, y, σ, t) are the spatial and time coordinates in the σ coordinate
 131 system. η is the free surface displacement and h is the still water level. After
 132 the σ transformation, the spatially filtered Navier-Stokes equations can be
 133 transformed to:

$$\frac{\partial u_1}{\partial x} + \frac{\partial u_1}{\partial \sigma} \frac{\partial \sigma}{\partial x^*} + \frac{\partial u_2}{\partial y} + \frac{\partial u_2}{\partial \sigma} \frac{\partial \sigma}{\partial y^*} + \frac{\partial u_3}{\partial \sigma} \frac{\partial \sigma}{\partial z^*} = 0 \quad (6)$$

$$\begin{aligned}
\frac{\partial u_1}{\partial t} + u_1 \frac{\partial u_1}{\partial x} + u_2 \frac{\partial u_1}{\partial y} + \omega \frac{\partial u_1}{\partial \sigma} = & -\frac{1}{\rho_f} \left(\frac{\partial p}{\partial x} + \frac{\partial p}{\partial \sigma} \frac{\partial \sigma}{\partial x^*} \right) + g_x + \frac{\partial \tau_{xx}}{\partial x} + \\
& \frac{\partial \tau_{xx}}{\partial \sigma} \frac{\partial \sigma}{\partial x^*} + \frac{\partial \tau_{xy}}{\partial y} + \frac{\partial \tau_{xy}}{\partial \sigma} \frac{\partial \sigma}{\partial y^*} + \frac{\partial \tau_{xz}}{\partial \sigma} \frac{\partial \sigma}{\partial z^*} - \\
& \frac{\partial \tau_{xx}^{SGS}}{\partial x} - \frac{\partial \tau_{xx}^{SGS}}{\partial \sigma} \frac{\partial \sigma}{\partial x^*} - \frac{\partial \tau_{xy}^{SGS}}{\partial y} - \\
& \frac{\partial \tau_{xy}^{SGS}}{\partial \sigma} \frac{\partial \sigma}{\partial y^*} - \frac{\partial \tau_{xz}^{SGS}}{\partial \sigma} \frac{\partial \sigma}{\partial z^*}
\end{aligned} \tag{7}$$

$$\begin{aligned}
\frac{\partial u_2}{\partial t} + u_1 \frac{\partial u_2}{\partial x} + u_2 \frac{\partial u_2}{\partial y} + \omega \frac{\partial u_2}{\partial \sigma} = & -\frac{1}{\rho_f} \left(\frac{\partial p}{\partial y} + \frac{\partial p}{\partial \sigma} \frac{\partial \sigma}{\partial y^*} \right) + g_y + \frac{\partial \tau_{yx}}{\partial x} + \\
& \frac{\partial \tau_{yx}}{\partial \sigma} \frac{\partial \sigma}{\partial x^*} + \frac{\partial \tau_{yy}}{\partial y} + \frac{\partial \tau_{yy}}{\partial \sigma} \frac{\partial \sigma}{\partial y^*} + \frac{\partial \tau_{yz}}{\partial \sigma} \frac{\partial \sigma}{\partial z^*} - \\
& \frac{\partial \tau_{yx}^{SGS}}{\partial x} - \frac{\partial \tau_{yx}^{SGS}}{\partial \sigma} \frac{\partial \sigma}{\partial x^*} - \frac{\partial \tau_{yy}^{SGS}}{\partial y} - \\
& \frac{\partial \tau_{yy}^{SGS}}{\partial \sigma} \frac{\partial \sigma}{\partial y^*} - \frac{\partial \tau_{yz}^{SGS}}{\partial \sigma} \frac{\partial \sigma}{\partial z^*}
\end{aligned} \tag{8}$$

$$\begin{aligned}
\frac{\partial u_3}{\partial t} + u_1 \frac{\partial u_3}{\partial x} + u_2 \frac{\partial u_3}{\partial y} + \omega \frac{\partial u_3}{\partial \sigma} = & -\frac{1}{\rho_f} \frac{\partial p}{\partial \sigma} \frac{\partial \sigma}{\partial z^*} + g_z + \frac{\partial \tau_{zx}}{\partial x} + \\
& \frac{\partial \tau_{zx}}{\partial \sigma} \frac{\partial \sigma}{\partial x^*} + \frac{\partial \tau_{zy}}{\partial y} + \frac{\partial \tau_{zy}}{\partial \sigma} \frac{\partial \sigma}{\partial y^*} + \frac{\partial \tau_{zz}}{\partial \sigma} \frac{\partial \sigma}{\partial z^*} - \\
& \frac{\partial \tau_{zx}^{SGS}}{\partial x} - \frac{\partial \tau_{zx}^{SGS}}{\partial \sigma} \frac{\partial \sigma}{\partial x^*} - \frac{\partial \tau_{zy}^{SGS}}{\partial y} - \\
& \frac{\partial \tau_{zy}^{SGS}}{\partial \sigma} \frac{\partial \sigma}{\partial y^*} - \frac{\partial \tau_{zz}^{SGS}}{\partial \sigma} \frac{\partial \sigma}{\partial z^*}
\end{aligned} \tag{9}$$

134 where

$$\omega = \frac{D\sigma}{Dt^*} = \frac{\partial \sigma}{\partial t^*} + u_1 \frac{\partial \sigma}{\partial x^*} + u_2 \frac{\partial \sigma}{\partial y^*} + u_3 \frac{\partial \sigma}{\partial z^*} \tag{10}$$

135 As for the shear stress τ_{ij} and sub-grid shear stress τ_{ij}^{SGS} ($i, j = 1, 2, 3$),
 136 they can be calculated as:

$$\tau_{ij} = \nu \left(\frac{\partial u_i}{\partial x_j} + \frac{\partial u_i}{\partial \sigma} \frac{\partial \sigma}{\partial x_j^*} + \frac{\partial u_j}{\partial x_i} + \frac{\partial u_j}{\partial \sigma} \frac{\partial \sigma}{\partial x_i^*} \right) \quad (11)$$

$$\tau_{ij}^{SGS} = -2\nu_t S_{ij} = -\nu_t \left(\frac{\partial u_i}{\partial x_j} + \frac{\partial u_i}{\partial \sigma} \frac{\partial \sigma}{\partial x_j^*} + \frac{\partial u_j}{\partial x_i} + \frac{\partial u_j}{\partial \sigma} \frac{\partial \sigma}{\partial x_i^*} \right) \quad (12)$$

137 where ν is the kinematic viscosity; ν_t is the eddy viscosity, which can be
 138 obtained from the Smagorinsky model [53] as:

$$\nu_t = (C_s \Delta)^2 \sqrt{2S_{ij}S_{ij}} \quad (13)$$

$$\Delta = (\Delta x_1 \Delta x_2 \Delta x_3)^{1/3} \quad (14)$$

139 where C_s is the Smagorinsky constant and should be calibrated and chosen
 140 based on the type of flow. In this study, the value is set to 0.2; Δ is a
 141 representative grid spacing and Δx_1 , Δx_2 , Δx_3 are the grid sizes in the
 142 coordinates of x^* , y^* , z^* , respectively.

143 2.2. Dispersed phase

144 The motion equation for a spherical particle within an unsteady and non-
 145 uniform fluid field is expressed as [24]:

$$\rho_p V_p \frac{d\mathbf{u}_p}{dt} = \mathbf{F}_b + \mathbf{F}_d + \mathbf{F}_p + \mathbf{F}_a + \mathbf{F}_{\text{Basset}} \quad (15)$$

146 where \mathbf{F}_b , \mathbf{F}_d , \mathbf{F}_p , \mathbf{F}_a , $\mathbf{F}_{\text{Basset}}$ are body force, drag force, fluid accelera-
 147 tion due to local pressure gradient, added mass force, Basset history force,
 148 respectively.

149 The body force \mathbf{F}_b acting on a single particle is calculated by

$$\mathbf{F}_b = (\rho_f - \rho_p) V_p \mathbf{g} \quad (16)$$

150 where ρ_p is the particle density; V_p is the volume of particle and \mathbf{g} is the
 151 gravitational acceleration.

152 The drag force \mathbf{F}_d is expressed as follows:

$$\mathbf{F}_d = -\frac{1}{2} \rho_f C_d A_p |\mathbf{u}_p - \mathbf{u}_f| (\mathbf{u}_p - \mathbf{u}_f) \quad (17)$$

153 where A_p is the projected area of a particle; \mathbf{u}_p is the particle velocity in
 154 three different directions; \mathbf{u}_f is the fluid velocity in three different directions;
 155 C_d is the drag coefficient, it is related with particle Reynolds number Re_p as
 156 follows:

$$C_d = f(Re_p) = \begin{cases} \frac{24}{Re_p} & , Re_p < 0.4 \\ \frac{24}{Re_p} (1 + 0.15Re_p^{0.687}) + \frac{0.42}{1+42500Re_p^{-1.16}} & , 0.4 \leq Re_p \leq 1000 \\ 0.45 & , Re_p > 1000 \end{cases} \quad (18)$$

$$Re_p = \frac{|\mathbf{u}_p - \mathbf{u}_f| d}{\nu} \quad (19)$$

157 where d is the particle diameter.

158 The fluid acceleration due to local pressure gradient force \mathbf{F}_p is formulated
 159 by:

$$\mathbf{F}_p = \rho_f V_p \left(\frac{d\mathbf{u}_f}{dt} \right)_f \quad (20)$$

160 The added mass force \mathbf{F}_a follows:

$$\mathbf{F}_a = \rho_f C_M V_p \left[\frac{d\mathbf{u}_p}{dt} - \left(\frac{d\mathbf{u}_f}{dt} \right)_f \right] \quad (21)$$

161 where C_M is the added mass coefficient and equals 0.5.

162 The Basset history force $\mathbf{F}_{\text{Basset}}$ here follows:

$$\mathbf{F}_{\text{Basset}} = -\frac{3}{2} d^2 \sqrt{\pi \rho_f \mu} \int_0^t \frac{\frac{d\mathbf{u}_r}{d\tau}}{\sqrt{t-\tau}} d\tau \quad (22)$$

163 where μ is the dynamic viscosity of fluid and $\mathbf{u}_r = \mathbf{u}_p - \mathbf{u}_f$ is the relative
 164 velocity between particle and fluid.

165 2.3. Problem setup and boundary conditions

166 The setup of the computational domain is shown in Figure 1. The di-
 167 mensions of the domain are L_x in length, L_y in width and L_z in depth. For
 168 wave cases, a numerical damping zone with a length of L_{x3} is switched on
 169 to reduce wave reflection. For cases involving a jet, a jet outlet boundary is

170 switched on. Additionally, the jet horizontal position is placed several meters
 171 upstream of the damping zone to maintain relatively stable flow conditions
 172 under wave conditions. A detailed description of the setup can be found in
 173 respective benchmark sections.

174 Six distinct boundary conditions, each corresponding to specific physical
 175 scenarios, are applied in this study. For the inflow boundary, both horizontal
 176 velocity $u_1(z, t)$, vertical velocity $u_3(z, t)$ and free surface displacement $\eta(t)$
 177 are given by analytical expressions [54] for wave cases as:

$$\begin{aligned} \eta(t) &= \frac{H}{2} \cos\left(\frac{\pi}{2} - \frac{2\pi}{T}t\right) + \frac{H^2k}{16} \frac{\cosh kh}{\sinh^3 kh} (2 + \cosh 2kh) \cos 2\left(\frac{\pi}{2} - \frac{2\pi}{T}t\right), -h \leq z \leq 0 \\ u_1(z, t) &= \frac{HgkT}{4\pi} \frac{\cosh k(h+z)}{\cosh kh} \cos\left(\frac{\pi}{2} - \frac{2\pi}{T}t\right) + \frac{3\pi H^2k}{8T} \frac{\cosh 2k(h+z)}{\sinh^4 kh} \cos 2\left(\frac{\pi}{2} - \frac{2\pi}{T}t\right), -h \leq z \leq 0 \\ u_3(z, t) &= \frac{HgkT}{4\pi} \frac{\sinh k(h+z)}{\cosh kh} \sin\left(\frac{\pi}{2} - \frac{2\pi}{T}t\right) + \frac{3\pi H^2k}{8T} \frac{\sinh 2k(h+z)}{\sinh^4 kh} \sin 2\left(\frac{\pi}{2} - \frac{2\pi}{T}t\right), -h \leq z \leq 0 \end{aligned} \quad (23)$$

178 where H is the wave height from the mean water level, k is the wave number,
 179 T is the period of oscillation and h is the initial water depth. The pressure at
 180 the inflow boundary is derived based on the assumption of negligible vertical
 181 acceleration at the free surface and is expressed as follows[41]:

$$\frac{\partial p}{\partial x} + \frac{\partial p}{\partial \sigma} \frac{\partial \sigma}{\partial x^*} = -\rho_f g_z \frac{\partial \eta}{\partial x}, \frac{\partial p}{\partial y} + \frac{\partial p}{\partial \sigma} \frac{\partial \sigma}{\partial y^*} = -\rho_f g_z \frac{\partial \eta}{\partial y} \quad (24)$$

182 For the bottom boundary, velocity gradients at the first interior node
 183 are estimated using the free-slip boundary condition. These gradients are
 184 then utilized in advection calculations. Meanwhile, the log-law wall function
 185 is used to calculate wall shear stress for the diffusion step for the bottom
 186 boundary. The pressure gradient in the normal direction follows a hydrostatic
 187 assumption:

$$\frac{\partial p}{\partial \sigma} = \rho_f (\eta + h) g_z \quad (25)$$

188 This approach yields satisfactory results with relatively coarse meshes, as
 189 evidenced by Lin and Liu [55]. At the front/back wall boundary, condi-
 190 tions similar to those for the bottom boundary are applied. For the outflow
 191 boundary, a zero-gradient condition is imposed on the velocity in the nor-
 192 mal direction, while the vertical pressure gradient follows the hydrostatic
 193 assumption.

194 For wave related cases, a numerical damping zone is applied at the out-
 195 flow boundary to minimize wave reflection. This zone replicates experimen-
 196 tal setups where breakwaters [56, 57] or porous structures [58] are commonly
 197 placed near the end of the flume to dissipate waves. By employing this ap-
 198 proach, surface waves are confined within the numerical channel, preventing
 199 artificial interactions with the boundary. The damping method utilized in
 200 this study can be expressed as [59]:

$$\phi_R = \phi + \Delta t \cdot \alpha \cdot \sigma \cdot \left(\frac{x - x_s}{x_e - x_s} \right)^2 \cdot (\phi - \phi_0) \quad (26)$$

201 where ϕ is the variable to be solved, such as u_i and η . ϕ_R is the resulting
 202 variable after the numerical damping; The empirical parameter α is assigned
 203 a value of -1.0 in this study. The subscripts 's' and 'e' represent the start
 204 and end points of the damping zone in the x -direction, respectively.

205 Finally, at the moving free surface η , the pressure is assumed to be equal
 206 to the air pressure(i.e., equal to zero). And the kinematic boundary condition
 207 is set as:

$$\frac{\partial \eta}{\partial t} + u_1 \frac{\partial \eta}{\partial x} + u_2 \frac{\partial \eta}{\partial y} - u_3 = 0 \quad (27)$$

208 The jet velocity boundary is generated by the Synthetic-Eddy-Method
 209 (SEM) outlined by Jarrin et al. [60]. The instantaneous velocities at the jet
 210 outlet are divided into the sum of a time-averaged part and a fluctuating part.
 211 The time-averaged velocity at each node matches the experiment performed
 212 by Lu and Yuan [61]. The fluctuating part of the velocity field at each grid
 213 point is given as:

$$u_i' = \frac{1}{\sqrt{N}} \sum_{i=1}^N \varepsilon_i f_\sigma(x_i - x) f_\sigma(y_i) \quad (28)$$

214 where

$$f_\sigma(\bar{x} - \bar{x}^k(t)) = \sqrt{\frac{V_B}{\sigma_x \sigma_y \sigma_z}} \cdot f\left(\frac{x - x^k(t)}{\sigma_x}\right) \cdot f\left(\frac{y - y^k(t)}{\sigma_y}\right) \cdot f\left(\frac{z - z^k(t)}{\sigma_z}\right) \quad (29)$$

215 The triangular function is written as

$$f(\zeta) = \begin{cases} \sqrt{1.5}(1 - |\zeta|) & |\zeta| \leq 1 \\ 0 & |\zeta| > 1 \end{cases} \quad (30)$$

216 Detailed description on the method can be found in Jarrin et al. [60].
 217 In this study, the fluctuation velocity and Reynolds stress distribution align
 218 with the DNS results conducted by Wu and Moin [62].

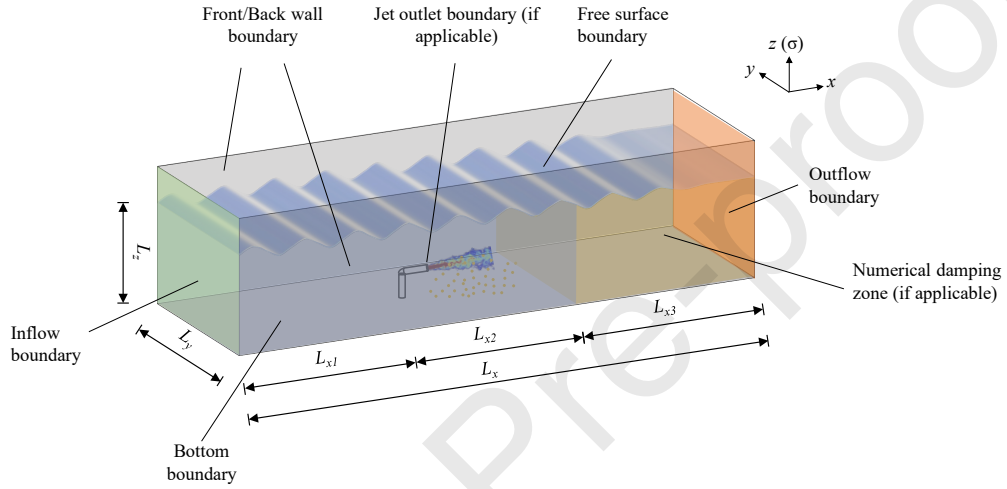


Figure 1: Computational domain and boundary conditions.

219 3. Numerical methods

220 3.1. Fluid phase

221 3.1.1. Numerical schemes for Navier-Stokes equations

222 An operator splitting technique [63, 64] is utilized for the numerical solu-
 223 tion of the governing equations. Within each time interval, the momentum
 224 equations are segmented into three separate steps, namely advection, diffu-
 225 sion, and pressure propagation [41]. For brevity, in this part, only governing
 226 equations in the horizontal direction will be presented below, equations in
 227 other directions can be solved in a similar way.

228 The finite difference form for the advection step is shown as:

$$\frac{(u_1)_{i,j,k}^{n+1/3} - (u_1)_{i,j,k}^n}{\Delta t} = - \left(u_1 \frac{\partial u_1}{\partial x} + u_2 \frac{\partial u_1}{\partial y} + \omega \frac{\partial u_1}{\partial \sigma} \right)_{i,j,k}^n \quad (31)$$

229 Equation (31) can be further split into following three sub-steps:

$$\begin{aligned}
\frac{(u_1)_{i,j,k}^{n+1/9} - (u_1)_{i,j,k}^n}{\Delta t} &= - \left(u_1 \frac{\partial u_1}{\partial x} \right)_{i,j,k}^n \\
\frac{(u_1)_{i,j,k}^{n+2/9} - (u_1)_{i,j,k}^{n+1/9}}{\Delta t} &= - \left(u_2 \frac{\partial u_1}{\partial y} \right)_{i,j,k}^{n+1/9} \\
\frac{(u_1)_{i,j,k}^{n+3/9} - (u_1)_{i,j,k}^{n+2/9}}{\Delta t} &= - \left(\omega \frac{\partial u_1}{\partial \sigma} \right)_{i,j,k}^{n+2/9}
\end{aligned} \tag{32}$$

230 To solve these above equations, the quadratic backward characteristic
231 method [65] and the Lax-Wendroff method are employed at the same time.
232 Final numerical results are calculated by using the average value on the above
233 two methods to ensure stability and accuracy, which can be written as:

$$(u_1)_{i,j,k}^{n+1/9} = \frac{\left[(u_1)_{i,j,k}^{n+1/9} \right]_{QC} + \left[(u_1)_{i,j,k}^{n+1/9} \right]_{LW}}{2} \tag{33}$$

234 where

$$\begin{aligned}
\left[(u_1)_{i,j,k}^{n+1/9} \right]_{QC} &= \frac{(\Delta x_{i-1} - \Delta x_a)(-\Delta x_a)}{\Delta x_{i-2}(\Delta x_{i-2} + \Delta x_{i-1})} (u_1)_{i-2,j,k}^n \\
&+ \frac{(\Delta x_{i-2} + \Delta x_{i-1} - \Delta x_a)(-\Delta x_a)}{(\Delta x_{i-2})(-\Delta x_{i-1})} (u_1)_{i-1,j,k}^n \\
&+ \frac{(\Delta x_{i-2} + \Delta x_{i-1} - \Delta x_a)(\Delta x_{i-1} - \Delta x_a)}{(\Delta x_{i-2} + \Delta x_{i-1})\Delta x_{i-1}} (u_1)_{i,j,k}^n
\end{aligned} \tag{34}$$

$$\begin{aligned}
\left[(u_1)_{i,j,k}^{n+1/9} \right]_{LW} &= \frac{\Delta x_a(\Delta x_i + \Delta x_a)}{\Delta x_{i-1}(\Delta x_{i-1} + \Delta x_i)} (u_1)_{i-1,j,k}^n \\
&+ \frac{(\Delta x_{i-1} - \Delta x_a)(-\Delta x_i - \Delta x_a)}{\Delta x_{i-1}(-\Delta x_i)} (u_1)_{i,j,k}^n \\
&+ \frac{(\Delta x_{i-1} - \Delta x_a)(-\Delta x_a)}{(\Delta x_{i-1} + \Delta x_i)\Delta x_i} (u_1)_{i+1,j,k}^n
\end{aligned} \tag{35}$$

235 In the above equations, the Δx_a is the advection distance and is defined
236 as $\Delta x_a = (u_1)_{i,j,k}^n \Delta t$.

237 In the diffusion step, the equation to be solved is as follows:

$$\frac{(u_1)_{i,j,k}^{n+2/3} - (u_1)_{i,j,k}^{n+1/3}}{\Delta t} = \left(\frac{\partial \tau_{xx}}{\partial x} + \frac{\partial \tau_{xx}}{\partial \sigma} \frac{\partial \sigma}{\partial x^*} + \frac{\partial \tau_{xy}}{\partial y} + \frac{\partial \tau_{xy}}{\partial \sigma} \frac{\partial \sigma}{\partial y^*} + \frac{\partial \tau_{xz}}{\partial \sigma} \frac{\partial \sigma}{\partial z^*} - \frac{\partial \tau_{xx}^{SGS}}{\partial x} - \frac{\partial \tau_{xx}^{SGS}}{\partial \sigma} \frac{\partial \sigma}{\partial x^*} - \frac{\partial \tau_{xy}^{SGS}}{\partial y} - \frac{\partial \tau_{xy}^{SGS}}{\partial \sigma} \frac{\partial \sigma}{\partial y^*} - \frac{\partial \tau_{xz}^{SGS}}{\partial \sigma} \frac{\partial \sigma}{\partial z^*} \right)_{i,j,k}^{n+1/3} \quad (36)$$

238 The stress term can be calculated according to Equation (11) and Equa-
 239 tion (12). The central difference is used to discretize all partial differentiation
 240 terms in the above equation as:

$$\left(\frac{\partial \tau_{xx}}{\partial x} \right)_{i,j,k}^{n+1/3} = \frac{(\tau_{xx})_{i+1/2,j,k}^{n+1/3} - (\tau_{xx})_{i-1/2,j,k}^{n+1/3}}{(\Delta x_{i-1} + \Delta x_i)/2} \quad (37)$$

241 where

$$(\tau_{xx})_{i+1/2,j,k}^{n+1/3} = (\nu + \nu_t) \left(\frac{(u_1)_{i+1,j,k}^{n+1/3} - (u_1)_{i,j,k}^{n+1/3}}{\Delta x_i} + \frac{(u_1)_{i+1/2,j,k+1}^{n+1/3} - (u_1)_{i+1/2,j,k-1}^{n+1/3}}{\Delta \sigma_{k-1} + \Delta \sigma_k} \left(\frac{\partial \sigma}{\partial x^*} \right)_{i+1/2,j,k}^{n+1/3} \right) \quad (38)$$

$$(\tau_{xx})_{i-1/2,j,k}^{n+1/3} = (\nu + \nu_t) \left(\frac{(u_1)_{i,j,k}^{n+1/3} - (u_1)_{i-1,j,k}^{n+1/3}}{\Delta x_{i-1}} + \frac{(u_1)_{i-1/2,j,k+1}^{n+1/3} - (u_1)_{i-1/2,j,k-1}^{n+1/3}}{\Delta \sigma_{k-1} + \Delta \sigma_k} \left(\frac{\partial \sigma}{\partial x^*} \right)_{i-1/2,j,k}^{n+1/3} \right) \quad (39)$$

242 In the above equations, $(u_1)_{i+1/2,j,k+1}^{n+1/3}$ means the velocity between nodes
 243 and can be obtained by the linear interpolation.

244 In the pressure propagation step, the following equation is to be solved:

$$\frac{(u_1)_{i,j,k}^{n+1} - (u_1)_{i,j,k}^{n+2/3}}{\Delta t} = -\frac{1}{\rho_f} \left(\frac{\partial p}{\partial x} + \frac{\partial p}{\partial \sigma} \frac{\partial \sigma}{\partial x^*} \right)_{i,j,k}^{n+1} + g_x \quad (40)$$

245 The central difference scheme in space is used to discretize the above two
 246 equations. To satisfy the continuity requirement, the resultant equation is
 247 incorporated into the continuity equation, leading to the derivation of the
 248 modified Poisson equation as follows:

$$\begin{aligned}
 & \left\{ \frac{\partial^2 p}{\partial x^2} + \frac{\partial^2 p}{\partial y^2} + \left[\left(\frac{\partial \sigma}{\partial x^*} \right)^2 + \left(\frac{\partial \sigma}{\partial y^*} \right)^2 + \left(\frac{\partial \sigma}{\partial z^*} \right)^2 \right] \frac{\partial^2 p}{\partial \sigma^2} \right. \\
 & \left. + 2 \left(\frac{\partial \sigma}{\partial x^*} \frac{\partial^2 p}{\partial x \partial \sigma} + \frac{\partial \sigma}{\partial y^*} \frac{\partial^2 p}{\partial y \partial \sigma} \right) + \left(\frac{\partial^2 \sigma}{\partial x^* \partial x} + \frac{\partial^2 \sigma}{\partial y^* \partial y} \right) \frac{\partial p}{\partial \sigma} \right\}_{i,j,k}^{n+1} \\
 & = \frac{\rho_f}{\Delta t} \left(\frac{\partial u}{\partial x} + \frac{\partial u}{\partial \sigma} \frac{\partial \sigma}{\partial x^*} + \frac{\partial v}{\partial y} + \frac{\partial v}{\partial \sigma} \frac{\partial \sigma}{\partial y^*} + \frac{\partial w}{\partial \sigma} \frac{\partial \sigma}{\partial z^*} \right)_{i,j,k}^{n+2/3}
 \end{aligned} \quad (41)$$

249 The CGSTAB method is used to solve the pressure Equation (41) dis-
 250 cretized using central differences [66].

251 3.1.2. Lagrangian-Eulerian method for tracking free surface

252 In order to get the surface elevation, The Lagrange–Euler method [66]
 253 is adopted in this study. Assume we have a particle which is at the free
 254 surface, the location of this particle at t_{n+1} is marked as $(x_{t_{n+1}}, y_{t_{n+1}})$ and
 255 we can also mark the corresponding particle position at t_n as (x_{t_n}, y_{t_n}) . By
 256 the Lagrange displacement equation and Taylor expansion, we can get the
 257 following equations:

$$\begin{aligned}
 x_{t_{n+1}} - x_{t_n} &= \int_{t_n}^{t_{n+1}} u_1(x(t), y(t), t) dt = u_1(x(t_\theta), y(t_\theta), t_\theta) \Delta t \\
 &= \left\{ u_{1,i,j}^{n+1} - \theta \left(\frac{\partial u_1}{\partial x} \right)_{i,j}^{n+1} (x_{t_{n+1}} - x_{t_n}) - \theta \left(\frac{\partial u_1}{\partial y} \right)_{i,j}^{n+1} (y_{t_{n+1}} - y_{t_n}) - \right. \\
 & \quad \left. \theta \left(\frac{\partial u_1}{\partial t} \right)_{i,j}^{n+1} \Delta t \right\} \Delta t
 \end{aligned} \quad (42)$$

$$\begin{aligned}
y_{t_{n+1}} - y_{t_n} &= \int_{t_n}^{t_{n+1}} u_2(x(t), y(t), t) dt = u_2(x(t_\theta), y(t_\theta), t_\theta) \Delta t \\
&= \left\{ u_{2i,j}^{n+1} - \theta \left(\frac{\partial u_2}{\partial x} \right)_{i,j}^{n+1} (x_{t_{n+1}} - x_{t_n}) - \theta \left(\frac{\partial u_2}{\partial y} \right)_{i,j}^{n+1} (y_{t_{n+1}} - y_{t_n}) - \right. \\
&\quad \left. \theta \left(\frac{\partial u_2}{\partial t} \right)_{i,j}^{n+1} \Delta t \right\} \Delta t
\end{aligned} \tag{43}$$

258 The central difference method for spatial derivatives and the forward
259 difference method for temporal derivatives are used to determine the variables
260 (x_{t_n}, y_{t_n}) by solving Equation (42) and Equation (43). Given the particle's
261 location within element (i, j) at time t_n , the initial surface elevation $\eta_{x,y}^n$
262 is interpolated from the grid node values within the element. Subsequently, the
263 Lagrange displacement equation is applied to update the surface elevation at
264 the subsequent time step $n + 1$.

$$\begin{aligned}
\eta_{i,j}^{n+1} &= \eta_{i,j}^n + \left\{ u_{3i,j}^{n+1} - \theta \left(\frac{\partial u_3}{\partial x} \right)_{i,j}^{n+1} (x_{t_{n+1}} - x_{t_n}) - \theta \left(\frac{\partial u_3}{\partial y} \right)_{i,j}^{n+1} (y_{t_{n+1}} - y_{t_n}) - \right. \\
&\quad \left. \theta \left(\frac{\partial u_3}{\partial t} \right)_{i,j}^{n+1} \Delta t \right\} \Delta t
\end{aligned} \tag{44}$$

265 3.1.3. Stability criteria

266 To ensure the stability and computational efficiency of this model, two
267 criteria must be met. The first criterion is related to the Courant-Friedrichs-
268 Lewy (CFL) condition, which is expressed as:

$$\Delta t \leq \beta \cdot \max \left(\frac{\Delta x_i}{(u_i)_{\max}} \right) \tag{45}$$

269 Here, $i = 1, 2, 3$ refers to the spatial dimensions (horizontal, transverse, and
270 vertical), with Δx_i representing the grid sizes and $(u_i)_{\max}$ denoting the max-
271 imum particle velocity in each respective direction. Although the theoretical

272 upper limit for β is 1.0, in practice, it is generally assigned a more conserva-
 273 tive value below 0.2 to maintain both stability and computational accuracy.
 274 In this model, the value is set to 0.1.

275 Another criterion applies to the diffusion term, which requires the follow-
 276 ing condition to be met:

$$\Delta t \leq \gamma \cdot \frac{(\Delta x_i)^2}{\nu} \quad (46)$$

277 where γ is typically assigned a value of 0.2. However, in most practical
 278 simulations, the time step is primarily constrained by the more restrictive
 279 CFL condition in Equation (45), as it imposes a tighter limit on the time
 280 step size due to the higher velocities encountered in the advection process.

281 3.2. Dispersed phase

282 When it comes to the dispersed phase, one main difficulty lies in how to
 283 get numerical solution of the Basset force, as the integrand is ill-behaved and
 284 would become an infinity when $\tau \rightarrow t$. To address this issue, the integral
 285 is divided into a series of small integrals, each calculated over a brief time
 286 step Δt . Assuming that the variation in relative velocity can be determined
 287 using the central difference method and that acceleration remains constant
 288 during Δt , the Basset integral can be computed as the cumulative total of
 289 these smaller integrals [67]. Hence, $\frac{d\mathbf{u}_r}{dt}$ is evaluated at the middle of the time
 290 step.

$$\begin{aligned}
 \mathbf{B} &= \int_0^{t+\Delta t} \frac{\frac{d\mathbf{u}_r}{d\tau}}{\sqrt{t+\Delta t-\tau}} d\tau \\
 &= \int_0^{\Delta t} \frac{\frac{d\mathbf{u}_r^0}{d\tau}}{\sqrt{t+\Delta t-\tau}} d\tau + \int_{\Delta t}^{2\Delta t} \frac{\frac{d\mathbf{u}_r^{\Delta t}}{d\tau}}{\sqrt{t+\Delta t-\tau}} d\tau + \dots + \int_{M\Delta t}^{M\Delta t+\Delta t} \frac{\frac{d\mathbf{u}_r^{M\Delta t}}{d\tau}}{\sqrt{t+\Delta t-\tau}} d\tau \\
 &= \frac{d\mathbf{u}_r^0}{d\tau} \int_0^{\Delta t} \frac{1}{\sqrt{t+\Delta t-\tau}} d\tau + \frac{d\mathbf{u}_r^{\Delta t}}{d\tau} \int_{\Delta t}^{2\Delta t} \frac{1}{\sqrt{t+\Delta t-\tau}} d\tau + \dots + \\
 &\quad \frac{d(\mathbf{u}_p - \mathbf{u}_f)}{d\tau} \int_{M\Delta t}^{M\Delta t+\Delta t} \frac{1}{\sqrt{t+\Delta t-\tau}} d\tau \\
 &= \frac{\mathbf{u}_{r,1} - \mathbf{u}_{r,0}}{\Delta t} \cdot 2(\sqrt{M\Delta t + \Delta t} - \sqrt{M\Delta t - \Delta t + \Delta t}) + \dots + \frac{\mathbf{u}_{r,M} - \mathbf{u}_{r,M-1}}{\Delta t} \cdot \\
 &\quad 2(\sqrt{M\Delta t - (M-1)\Delta t + \Delta t} - \sqrt{M\Delta t - M\Delta t + \Delta t}) + 2\sqrt{\Delta t} \frac{d(\mathbf{u}_p - \mathbf{u}_f)}{dt} \\
 &= \frac{2}{\sqrt{\Delta t}} \sum_{n=0}^{M-1} \left[(\mathbf{u}_{r,n+1} - \mathbf{u}_{r,n}) \left(\sqrt{M-n+1} - \sqrt{M-n-1+1} \right) \right] + 2\sqrt{\Delta t} \frac{d(\mathbf{u}_p - \mathbf{u}_f)}{dt} \\
 &= \mathbf{B}_0^t + 2\sqrt{\Delta t} \frac{d(\mathbf{u}_p - \mathbf{u}_f)}{dt}
 \end{aligned} \tag{47}$$

291 where \mathbf{B}_0^t is the Basset integral between $\tau=0$ to t .

292 At $\tau = t$, the simplified version of Equation (15) can be written as

$$\frac{d\mathbf{u}_p}{dt} = \frac{\left[(1-s)g + (1+C_M) \left(\frac{d\mathbf{u}_f}{dt} \right)_f - \frac{3C_D}{4d} |\mathbf{u}_p - \mathbf{u}_f| (\mathbf{u}_p - \mathbf{u}_f) - \frac{9}{d} \sqrt{\frac{\nu}{\pi}} \mathbf{B}_0^t \right]}{(s+C_M)} = \mathbf{F} \tag{48}$$

293 While when $\tau = t + \Delta t$, after applying the Equation (47), the governing
 294 equation can be written as

$$\frac{d\mathbf{u}_p}{dt} = \frac{\left[(1-s)g + (1+C_M + \frac{18}{d} \sqrt{\frac{\nu}{\pi}} \Delta t) \left(\frac{d\mathbf{u}_f}{dt} \right)_f - \frac{3C_D}{4d} |\mathbf{u}_p - \mathbf{u}_f| (\mathbf{u}_p - \mathbf{u}_f) - \frac{9}{d} \sqrt{\frac{\nu}{\pi}} \mathbf{B}_0^t \right]}{(s+C_M + \frac{18}{d} \sqrt{\frac{\nu}{\pi}} \Delta t)} \tag{49}$$

295 At the N th time step, the particle position $\mathbf{x}_{p,N}$, particle velocity $\mathbf{u}_{p,N}$,
 296 and flow velocity $\mathbf{u}_{f,N}$ are known. Initially, a preliminary estimate for the

297 particle velocity $\mathbf{u}_{\mathbf{p},N+1} = \mathbf{u}_{\mathbf{p},N} + \Delta t \times \mathbf{F}(\mathbf{u}_{\mathbf{p},N}, \mathbf{x}_{\mathbf{p},N})$ is made at $\tau = t + \Delta t$,
 298 enabling the calculation of the corresponding particle position $\mathbf{x}_{\mathbf{p},N}$. Subse-
 299 quently, a second-order implicit iteration method is employed to determine
 300 the particle's velocity and position at the $(N + 1)$ th time step. This iterative
 301 process continues until the relative deviation between two successive itera-
 302 tions is less than 0.1%. Ultimately, the final particle velocity and position are
 303 obtained. It is noteworthy that this numerical method is applicable beyond
 304 situations where the Basset force is considered. In scenarios where the Bas-
 305 set force is excluded, the term \mathbf{B}_0^t can be disregarded, and the equations in
 306 Equation (48) can be further simplified. The detailed numerical scheme for
 307 solving the governing equation of the dispersed phase is outlined in Algorithm
 308 1.

Algorithm 1 Numerical method for dispersed phase

```

1:  $\mathbf{u}_{\mathbf{p},N+1}^{(0)} \leftarrow \mathbf{u}_{\mathbf{p},N} + \Delta t * \mathbf{F}(\mathbf{u}_{\mathbf{p},N}, \mathbf{x}_{\mathbf{p},N}), \mathbf{x}_{\mathbf{p},N+1}^{(0)} \leftarrow \mathbf{x}_{\mathbf{p},N} + \Delta t * \mathbf{u}_{\mathbf{p},N+1}^{(0)}$ 
2: while  $[\mathbf{u}_{\mathbf{p},N+1}^{(k+1)} - \mathbf{u}_{\mathbf{p},N+1}^{(k)}] / \mathbf{u}_{\mathbf{p},N+1}^{(k)} \geq 10^{-3}$  do
3:    $\mathbf{u}_{\mathbf{p},N+1}^{(k+1)} \leftarrow \mathbf{u}_{\mathbf{p},N} + \frac{\Delta t}{2} * [\mathbf{F}(\mathbf{u}_{\mathbf{p},N}, \mathbf{x}_{\mathbf{p},N}) + \mathbf{F}(\mathbf{u}_{\mathbf{p},N+1}^{(k)}, \mathbf{x}_{\mathbf{p},N+1}^{(k)})];$ 
    $\mathbf{x}_{\mathbf{p},N+1}^{(k+1)} \leftarrow \mathbf{x}_{\mathbf{p},N} + \mathbf{u}_{\mathbf{p},N+1}^{(k+1)} * \Delta t, k = 0, 1, 2, \dots$ 
4: end while
5:  $\mathbf{u}_{\mathbf{p},N+1} \leftarrow \mathbf{u}_{\mathbf{p},N+1}^{(k+1)}, \mathbf{x}_{\mathbf{p},N+1} \leftarrow \mathbf{x}_{\mathbf{p},N+1}^{(k+1)}$ 

```

309 *3.3. Solution procedure*

310 In order to make the solution procedure of the model a more direct and
 311 easier to understand, a flow chart is presented in Figure 2.

- 312 1. Calculate $u_i^{n+1/3}$ ($i = 1, 2, 3$) at advection step from Equations (31)-
 313 (35).
- 314 2. Solve Equations (36) to obtain $u_i^{n+2/3}$ ($i = 1, 2, 3$) in the diffusion step.
- 315 3. Use the Conjugate Gradient Squared (CGSTAB) method to solve Equa-
 316 tion (41) for the pressure field p^{n+1} and velocity u_i^{n+1} .
- 317 4. Calculate the free surface displacement η^{n+1} using Equation (44).
- 318 5. Get the particle positions and velocities from Equation (49), based on
 319 the flow velocities derived in Steps 1-3.

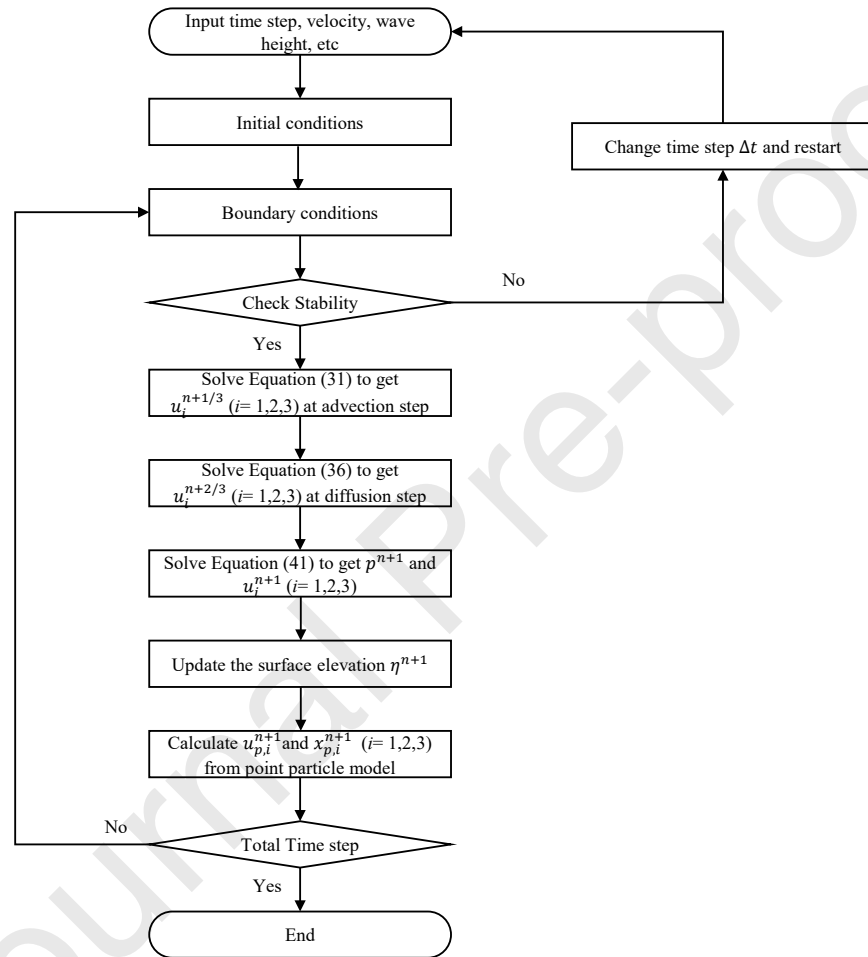


Figure 2: Solution procedure of the model.

320 4. Results and discussion

321 4.1. Benchmark: non-hydrostatic wave flume

322 4.1.1. Regular waves

323 A regular progressive wave is generated in the non-hydrostatic wave flume,
 324 as depicted in Figure 1. The dimensions of the flume are $L_x = 15$ m in length,
 325 $L_y = 0.5$ m in width, and $L_z = 0.5$ m in depth. The damping zone has a
 326 length of $L_{x3} = 5$ m and is positioned at the end of the flume to dissipate
 327 wave energy. The amplitude of the regular wave is 0.02 m and the wave
 328 period is 1 s.

329 Eight different grid systems, as detailed in Table 1, are performed to
 330 check the spatial convergence of the model. Grid1 to Grid4 focus on spatial
 331 convergence in the horizontal direction, while Grid2 and Grid5 to Grid8 are
 332 employed for the convergence in the vertical direction. For the transverse
 333 direction, the inflow condition of the water level along this direction is the
 334 same and as discussed in Section 2.3, a zero-gradient condition is applied
 335 to the wall's normal direction. The discretization in the y -direction does
 336 not influence changes in the water level η . Hence, fixed grids are set in the
 337 transverse direction for all the cases. The grids are uniformly distributed
 338 in both horizontal and vertical directions. The normalized L_1 error E_{L_1} ,
 339 L_2 error E_{L_2} , and maximum error E_{L_∞} were used in this test, which were
 340 calculated as follows:

$$E_{L_1} = \frac{\sum |\eta_{numerical} - \eta_{analytical}|}{n} \quad (50)$$

$$E_{L_2} = \sqrt{\frac{\sum (\eta_{numerical} - \eta_{analytical})^2}{n}} \quad (51)$$

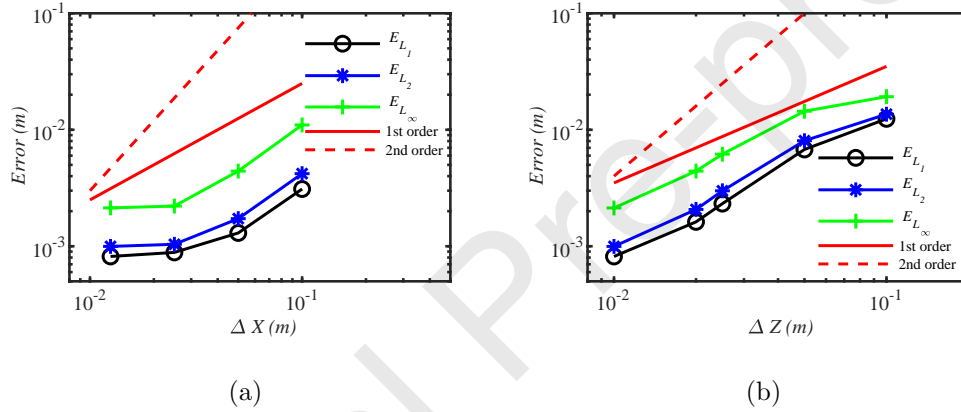
$$E_{L_\infty} = \max |\eta_{numerical} - \eta_{analytical}| \quad (52)$$

341 In Grid systems 1–4, the water depth is discretized using 100 uniform
 342 grids, while the horizontal direction is discretized with varying uniform grids.
 343 As shown in Figure 3(a), the convergence order in the horizontal direction
 344 approaches first-order accuracy. Similarly, Figure 3(b) demonstrates that
 345 the convergence order in the vertical direction is also close to the first order.
 346 Finally, Grid-3 was selected for the simulation in this case.

347 Figure 4 shows the spatial profiles of water level throughout the entire
 348 flume at $t = 25$ s, as well as the temporal profile of water level at $x = 6$ m.

Table 1: Grid systems of spatial convergence study on regular waves.

Grid	Grid points	min Δx	min $\Delta \sigma$
Grid-1	151x11x101	0.1 m	0.01
Grid-2	301x11x101	0.05 m	0.01
Grid-3	601x11x101	0.025 m	0.01
Grid-4	1201x11x101	0.0125 m	0.01
Grid-5	301x11x51	0.05 m	0.02
Grid-6	301x11x41	0.05 m	0.025
Grid-7	301x11x21	0.05 m	0.05
Grid-8	301x11x11	0.05 m	0.1

Figure 3: Spatial convergence study of regular waves along the whole flume at $t=25$ s: (a) horizontal direction; (b) vertical direction.

349 Evidently, the numerical results match well with analytical solutions. Ad-
 350 ditionally, Figure 4(a) demonstrates that wave reflection is negligible within
 351 the effective zone (0 m-10 m), which proves that wave energy was dissipated
 352 effectively in the damping zone (10 m-15 m). Figure 5 shows the relative
 353 volume of water over time for regular waves. It can be seen that the volume
 354 of water preserves well and stabilizes after 30 seconds, which confirms the
 355 validity of the model.

356 Figure 6 shows the maximum horizontal velocity distribution and maxi-
 357 mum vertical velocity distribution along water depth in one wave period and
 358 their comparison with analytical solutions at $x = 6$ m. The comparison of
 359 horizontal and vertical velocity distributions with analytical results reveals

360 negligible differences, indicating the flow field is well simulated. It is worth
 361 mentioning that a slight difference in the horizontal velocity can be seen in
 362 Figure 6 close to the bottom, and this can be attributed to the wave bound-
 363 ary layer which exists at a very narrow range close to the bottom. Due to the
 364 existence of the boundary layer, the real velocity distribution would deviate
 365 from the analytical solution close to the bottom. In addition, the veloc-
 366 ity should equal zero at the bottom, which is consistent with our numerical
 367 results. In summary, the numerical model successfully replicates both the
 368 water surface changes and the velocity distribution of regular waves.

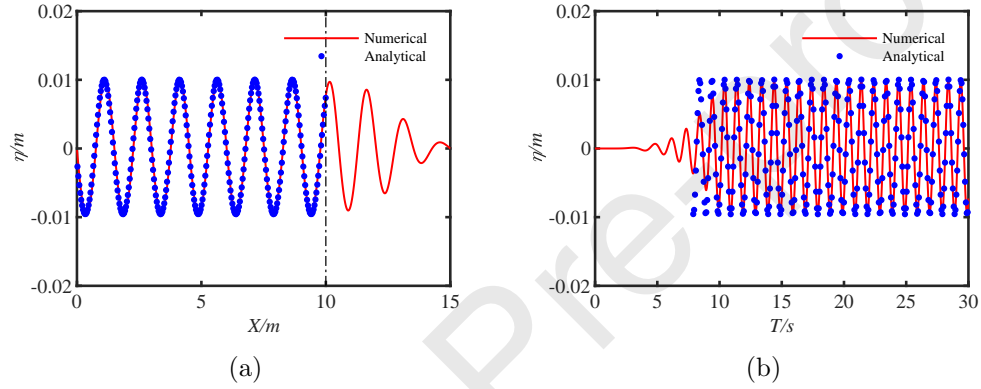


Figure 4: Free surface verification for the regular waves: (a) Spatial distribution of water level along the whole flume at $t = 25$ s; (b) Temporal distribution of water level at $x = 6$ m.

369 4.1.2. Wave-structure interaction

370 When a regular wave encounters a submerged bar, it frequently experi-
 371 ences significant changes in the waveform, resulting in noteworthy nonlinear
 372 energy interactions among various wave modes [41]. The simulation of such
 373 case is imperative, as it serves as a foundational test case for numerical tanks
 374 and can yield critical insights into the dynamics of wave interactions with
 375 submerged structures.

376 Our numerical simulations are based on experiments conducted by Beji
 377 and Battjes [68]. The geometry of our numerical computations is depicted in
 378 Figure 7. The length of the flume is 30 m, the width is 0.5 m and the water
 379 depth is 0.4 m. A regular wave with a wave height of 0.02 m and a period
 380 of 2 s is generated from the inflow boundary and the damping zone L_{x3} is

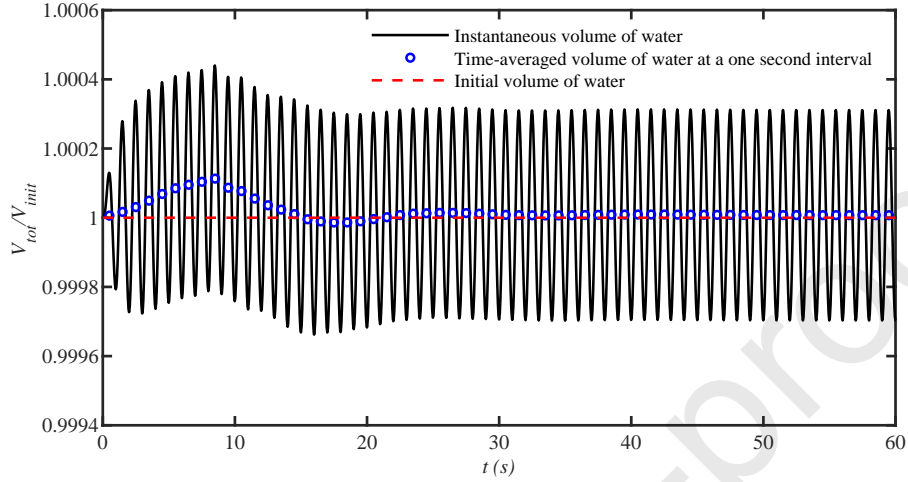


Figure 5: Relative volume of water over time for the regular waves.

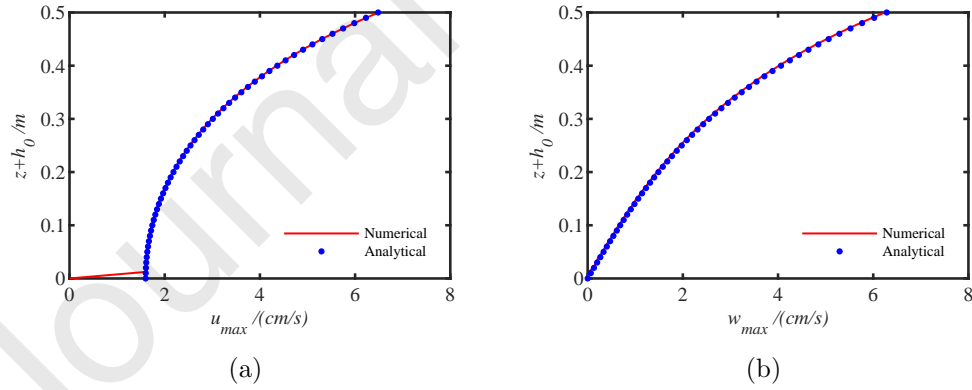


Figure 6: Verification of the velocity distribution of a regular wave, (a) the horizontal velocity distribution along water depth in wave peak phase; (b) the vertical velocity distribution along water depth in up-zero crossing phase.

381 set as 10 m to dissipate the wave energy. Seven wave gauges are positioned
 382 at various locations within the flume. To ensure grid convergence, seven
 383 different grid configurations are employed in the model (as shown in Table
 384 2), with a time step of $\Delta t = 0.005$ s. The simulations were carried out on
 385 a desktop computer with an AMD Ryzen(TM) 5 5600X CPU and 16GB
 386 internal memory. The base frequency of this CPU is 3.7 GHz. The total
 387 CPU time per time step required for the present model was about 1.8 s.

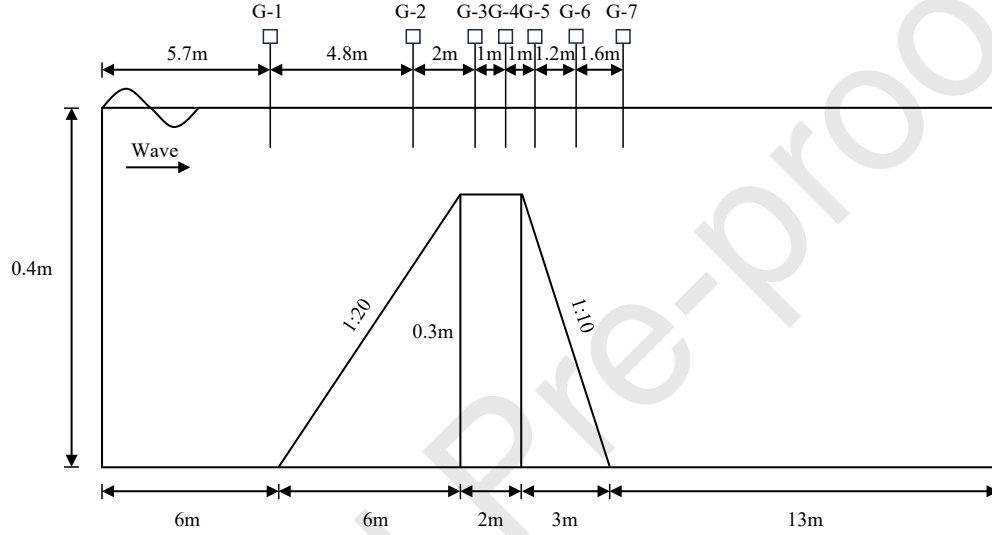


Figure 7: Sketch of the geometry for a regular wave passing the submerged bar. PS: G stands for wave gauges.

Table 2: Mesh convergence study on wave-structure interaction.

Grid	Grid points	min Δx	min Δy	min $\Delta \sigma$
Grid-1	1201x9x47	0.025 m	0.05 m	0.011
Grid-2	2401x5x47	0.0125 m	0.10 m	0.011
Grid-3	2401x9x24	0.0125 m	0.05 m	0.022
Grid-4	2401x9x47	0.0125 m	0.05 m	0.011
Grid-5	2401x9x93	0.0125 m	0.05 m	0.0055
Grid-6	2401x17x47	0.0125 m	0.025 m	0.011
Grid-7	4801x9x47	0.00625 m	0.05 m	0.011

388 The comparisons between our numerical findings and the gauge data for
 389 free surface elevation at six designated locations are depicted in Figure 8.

390 The results from seven different grid systems are also presented in the figure.
 391 For most grid systems, the numerical simulation results match well with the
 392 experimental data, except for Grid-3, where a distinct phase lag is observed.
 393 This discrepancy can be attributed to the relatively low grid resolution at
 394 the free surface. Ultimately, Grid-4 is selected for the simulation in this
 395 case. It was found that at wave gauge 2 ($x = 10.5$ m), the wave retains
 396 its sinusoidal feature, displaying strong concurrence between the numerical
 397 results and experimental data. Moving from $x = 10.5$ m to $x = 12.5$ m, we
 398 observe the wave deformation as it climbs the slope. From wave gauge 4 (x
 399 $= 13.5$ m) to 7 ($x = 17.5$ m), where the wave surmounts the breakwater,
 400 exhibit the emergence of secondary wave growth.

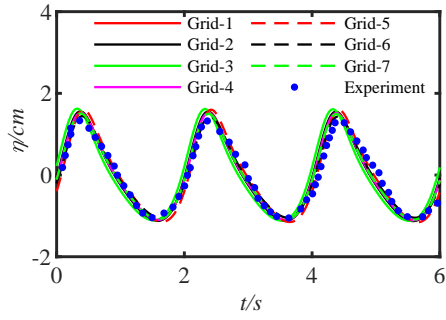
401 Figure 9 shows the top and side view plots of the 3D free surface elevation
 402 at a representative time. The red, yellow, black, and blue rectangle repre-
 403 sents the upslope part, horizontal part, downslope part, and damping zone,
 404 respectively. It can be seen that the wavelength gradually decreases while the
 405 wave height increases during the wave shoaling process. On the contrary, a
 406 decrease in wave height is observed when the wave moves downhill, and more
 407 small waves can be seen. It can be attributed to the dissipation in wave en-
 408 ergy which in return lead to the generation of higher-order secondary waves.
 409 In summary, the numerical model accurately captures this progression, al-
 410 though minor disparities in the variation of wave height exist between the
 411 numerical results and experimental data. These distinctions may arise from
 412 numerical dissipation and the σ transformation, stemming from the abrupt
 413 change in water depth.

414 4.2. Benchmark: point particle

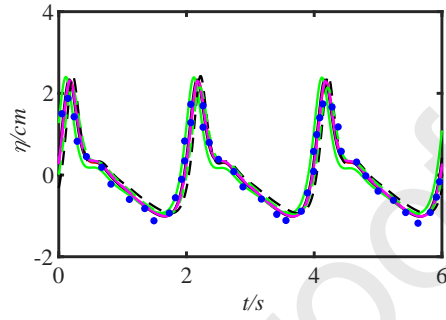
415 To validate the point-particle model, the accelerated process of a spher-
 416 ical particle settling in a stationary fluid is simulated. When the particle
 417 Reynolds number Re_p is relatively small (i.e., $Re_p < 0.4$), the analytical so-
 418 lution of the acceleration process can be derived from linear (Stokes) drag
 419 law. By neglecting the Basset history term and assuming an initial velocity
 420 of zero, we can derive the temporal evolution of particle velocity as follows:

$$w_p(t) = \frac{(s-1)gd^2}{18\nu} \left(1 - e^{-\frac{18\nu t}{d^2(s+CM)}} \right) \quad (53)$$

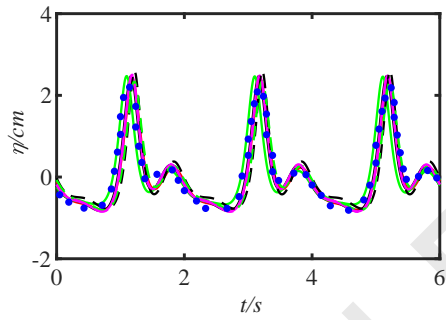
421 When the Basset force is considered, the analytical solution can be found
 422 in Brush et al. [69] in a closed-form solution:



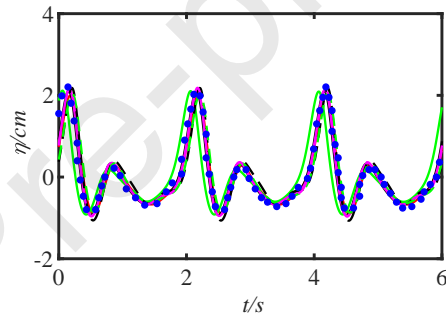
(a) Gauge 2



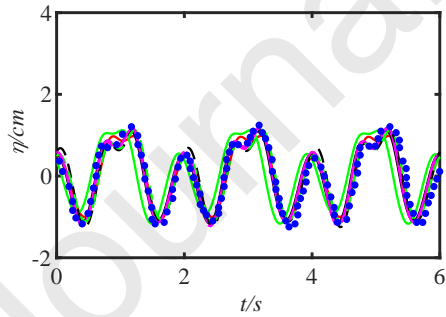
(b) Gauge 3



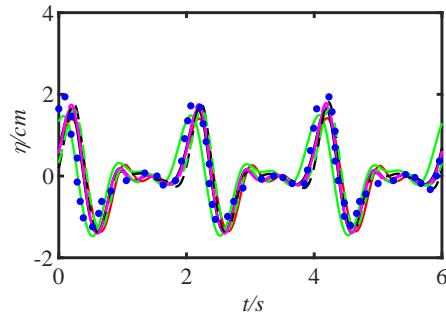
(c) Gauge 4



(d) Gauge 5



(e) Gauge 6



(f) Gauge 7

Figure 8: Comparison of the elevation between numerical results and experiment results at six different gauge points.

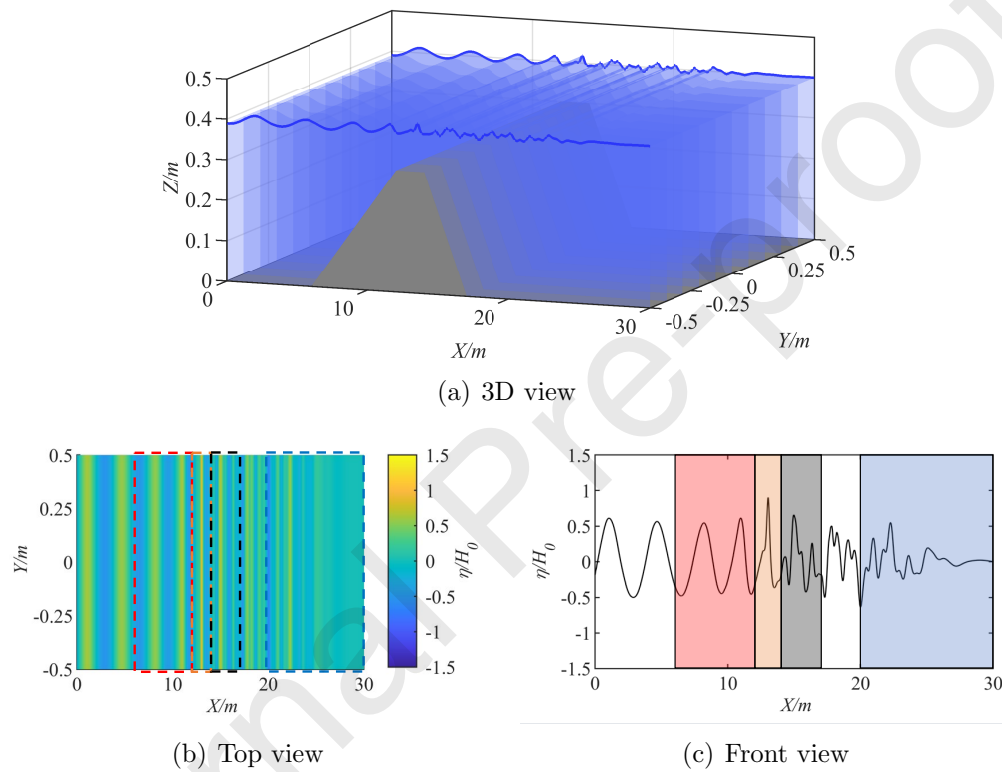


Figure 9: The surface elevation of regular wave interacts with submerged bar. (a) 3D view (b) top view (c) Front view of free surface elevation changes at representative time (Red rectangle: 1:20 upslope; Yellow rectangle: horizontal crest; Black rectangle: 1:10 downslope; Blue rectangle: damping zone).

$$w_p(t) = \frac{(s-1)gd^2}{18\nu} \left\{ 1 + \frac{\sqrt{c^2+h^2}}{h} \exp(-h^2t) \left[\exp(c^2t) \sin(2cht - \alpha) \operatorname{erfc}(c\sqrt{t}) - 2\sqrt{\frac{t}{\pi}} \int_0^h \exp(y^2t) \cos[2c(h-y)t - \alpha] dy \right] \right\} \quad (54)$$

423 where

$$c = \frac{9\sqrt{\nu}}{2d(s+C_M)} \quad (55)$$

$$h = \frac{3}{2d(s+C_M)} \sqrt{\nu[8(s+C_M) - 9]} \quad (56)$$

$$\alpha = \tan^{-1} \left(\frac{h}{c} \right) \quad (57)$$

424 and $\operatorname{erfc}(t)$ is the complementary error function, which writes as:

$$\operatorname{erfc}(t) = \frac{2}{\sqrt{\pi}} \int_t^\infty \exp(-t^2) dt \quad (58)$$

425 Figure 10(a) shows the comparison of analytical and numerical solutions
 426 of the motion of a $50 \mu\text{m}$ diameter sphere falling in water with the param-
 427 eters $\rho_p = 2500 \text{ kg/m}^3$, $s = \rho_p/\rho_f = 2.5$, kinematic viscosity $\nu = 10^{-6} \text{ m}^2/\text{s}$
 428 and particle Reynolds number $Re_p = 0.1$. As it takes very short time for a
 429 single particle to reach its terminal settling velocity, the time step is set as
 430 $\Delta t = 0.0001 \text{ s}$. Significant differences can be observed when Basset force was
 431 considered or not. Without the Basset force, the particle reaches its settling
 432 velocity fast; while the particle accelerates at a much slower rate when Bas-
 433 set force is considered. It can also be clearly seen that the numerical results
 434 match well with the analytical solution.

435 As mentioned before, the analytical solution of the settling process of a
 436 round particle is only applicable to the linear (Stokes) drag law, experiments
 437 performed by Mordant et al. [70] are further adopted to validate the applica-
 438 bility of the point particle model in non-linear drag range. The sphere diam-
 439 eter used in the experiment is $500 \mu\text{m}$, $s = \rho_p/\rho_f = 2.565$, $\nu = 9.0366 \times 10^{-7}$
 440 m^2/s , particle Reynolds number $Re_p = 41$ and the time step is set as $\Delta t = 0.00005$

441 s. It can be found from Figure 10(b) that the numerical results match better
 442 with experimental data when the Basset force is considered. Both the early
 443 stage of particle settling and the terminal settling velocity correspond well
 444 to the experiments.

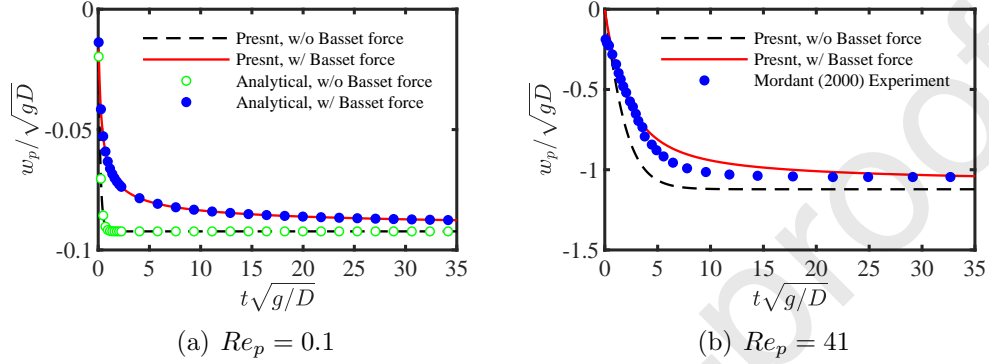


Figure 10: Accelerated process of a spherical particle settle in a stationary liquid, (a) $Re_p = 0.1$; (b) $Re_p = 41$.

445 4.3. Benchmark: Single particle in an oscillating liquid

446 Given the good agreement between our simulated settling process of a
 447 single particle in a stationary liquid, our attention now shifts to simulat-
 448 ing settling process of a single particle in vertically oscillating liquid. The
 449 data are adapted from experiments done by Ho [71]. The experiments were
 450 conducted in a cylinder which was filled with fluids, and it would oscillate
 451 vertically with different amplitudes and frequencies as follows:

$$w_f(t) = w_{f0} \sin(\omega t) \quad (59)$$

452 where w_{f0} is the velocity oscillation amplitude; $\omega = 2\pi/T$ is the angular
 453 frequency and T is the oscillation period. The particle motion process is
 454 computed for several oscillation cycles until the velocity deviation between
 455 two consecutive periods is less than 0.1%. The average settling velocity ω_{sa}
 456 is computed by averaging the velocities in an oscillation cycle. The time
 457 step is set as $\Delta t = 0.00005$ s. Four different Re_p and two different oscillation
 458 periods are chosen. In total 8 cases are simulated. Detailed parameters used
 459 in the 8 cases are summarized in Table 3.

Table 3: Summary of different cases on sphere settling in oscillation field.

Case	Re_p	Diameter μm	s ρ_p/ρ_f	Viscosity 10^{-6} m^2/s	Oscillation period s	$\nu/d^2\omega_s$
1	0.18	1587	6.27	250.80	0.15	2.3
2	0.18	1587	6.27	250.80	0.19	3.0
3	1.1	3175	6.16	250.80	0.15	0.59
4	1.1	3175	6.16	250.80	0.19	0.74
5	6	1587	6.53	35.77	0.15	0.330
6	6	1587	6.53	35.77	0.19	0.430
7	28	3175	6.41	35.77	0.15	0.085
8	28	3175	6.41	35.77	0.19	0.110

460 Figure 11 shows the comparison between the simulated non-dimensional
461 averaged settling velocity and oscillation acceleration ratio with experiments.
462 The results depicted by the solid lines in Figure 11 are obtained through a
463 sequence of simulations, all maintaining the constant frequency while the
464 wave amplitudes are systematically varied. Following these simulations, the
465 oscillation acceleration ratios for each amplitude are computed and the rela-
466 tion between the wave amplitudes and the oscillation acceleration ratios are
467 drawn into solid lines in this figure. It can be seen from these figures that
468 with the increase of the oscillation amplitude, the non-dimensional averaged
469 settling velocity would decrease. This reduction in settling velocity can be
470 attributed to the enhanced particle inertia during the oscillating motion of
471 the fluid, which, when increased, tends to overpower the effects of viscosity
472 around the particle and can lead to a more distinct decrease in averaged
473 settling velocity. Another interesting finding is that when the Basset force
474 is considered in the settling process, the numerical simulation results devi-
475 ate more than when the Basset force is not considered. One of the reasons
476 lies in that the Basset force is applicable in relatively small particle Reynolds
477 number and is inapplicable to high particle Reynolds number conditions [24];
478 Also the Basset force can be considered as a kind of viscous force and would
479 resist the movement of the particle. As a result, the average settling veloc-
480 ity in one oscillation period would decrease when Basset force is considered.
481 Finally, we can conclude that the numerical simulation results match better
482 with experiments without Basset force. As the wave field can be seen as a

483 specific oscillation flow, we would not consider the Basset force in our later
 484 simulation on sediment-laden jet in flow with waves.

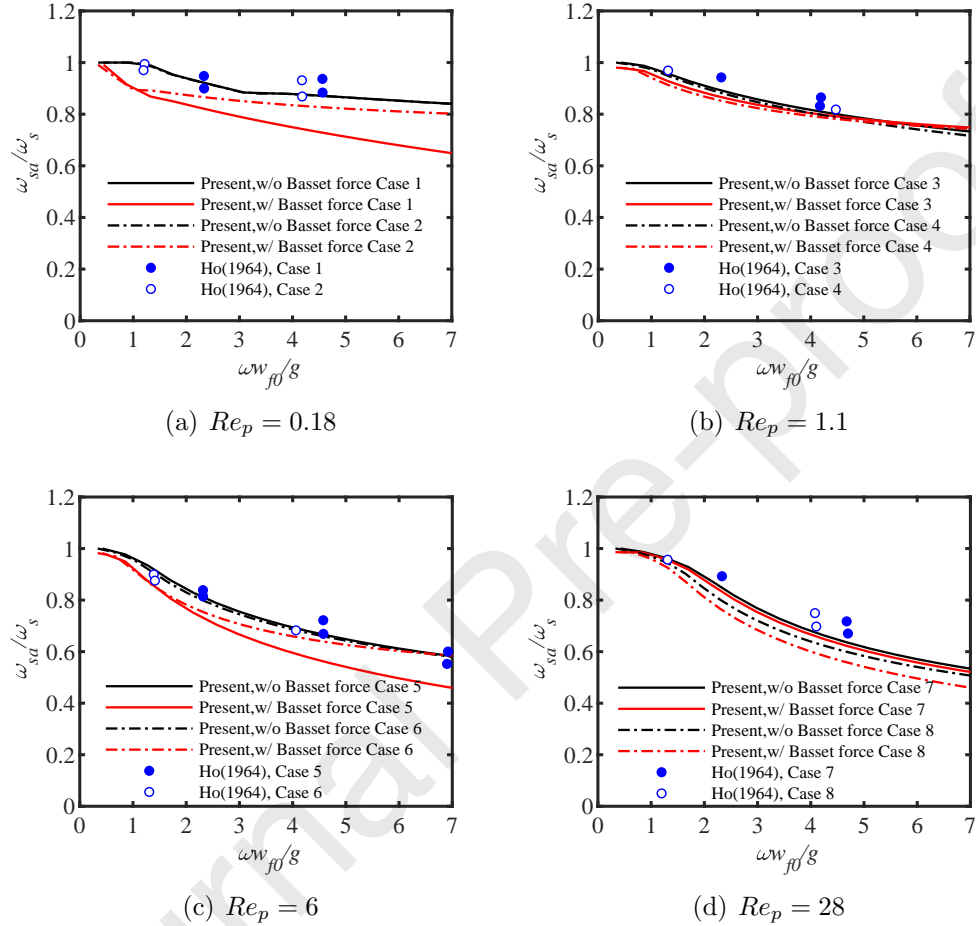


Figure 11: Comparison of the numerical model and the experimental of Ho [71] of accelerated process of a spherical particle settle in oscillation field.

485 4.4. Benchmark: sediment-laden jet in a stationary environment

486 To check the capability of the coupled model between the non-hydrostatic
 487 model and the point-particle model, we choose to simulate the sediment-laden
 488 jet in a stationary environment. The setup of the experiment is the same as
 489 the experiments performed by Chen et al. [72]. The tank has a length of 1.5

490 m, a width of 0.5 m, and a height of 0.6 m. The tank keeps a depth of 0.5
491 m. The diameter of the jet orifice is 0.01 m and is located 0.15 m above the
492 collection tray. The computational domain is discretized into $131 \times 41 \times 139$
493 grids. A non-uniform grid is implemented, and refined at the jet orifice, with
494 minimum grid sizes in the x , y , and σ directions of 0.001 m. The time step is
495 set to 0.002 s and the total CPU time per time step required for the present
496 model was approximately 4.3 s. The jet outlet velocity is set as 0.76 m/s and
497 the velocity boundary is specified using the SEM (Synthetic-Eddy-Method)
498 method. Given that the volume concentration of the simulated sediment-
499 laden jet is below 0.1%, only one-way coupling is considered [73], where both
500 the reaction of particles to the flow field and interactions among particles are
501 neglected.

502 Figure 12 shows the comparison of centerline velocity decay and axial ve-
503 locity distribution between experimental and numerical results. To check the
504 mesh convergence at the jet outlet boundary, the jet outlet was discretized
505 by 8×8 , 10×10 and 12×12 grids, respectively. It is found that the centerline
506 velocity decay is similar when the jet outlet boundary is discretized by finer
507 grids like Grid 10-10 and Grid 12-12. Therefore, the 10×10 grid was selected
508 for the jet outlet boundary. Additionally, it is found that the simulation
509 results match well with the experiments by Kwon and Seo [74]. When it
510 comes to velocity distribution in cross-sections, it is found that the distribu-
511 tion follows the Gaussian distribution at cross-sections in self-similar zone.
512 In conclusion, the accuracy of the flow field was verified.

513 We present 3D visualizations of the instantaneous and time-averaged iso-
514 surfaces of a jet in a stationary environment (see Figure 13). The isosurfaces
515 represent velocities ranging from 0.2 m/s to 0.8 m/s, with intervals of 0.2
516 m/s. Figure 13(a) shows the velocity distribution of the jet at a specific time,
517 where the isosurface appears irregular, reflecting the fluctuating structures
518 caused by the inherent unsteadiness and turbulence of the flow. In contrast,
519 the time-averaged velocity isosurface (see Figure 13(b)) appears smoother
520 than the instantaneous one. The shapes and behavior of both instantaneous
521 and time-averaged isosurfaces are consistent with previous studies on turbu-
522 lent jets in stationary environments, thereby validating the accuracy of the
523 numerical simulation model.

524 The particles used in the numerical simulation have a median size $D_{50} =$
525 $200 \mu\text{m}$. As shown in Figure 14(a), the actual diameter distribution follows
526 the distributions used in experiments, which was measured using the Laser
527 Diffraction Particle Size Analyzer (Malvern Mastersizer 3000). A total of 8

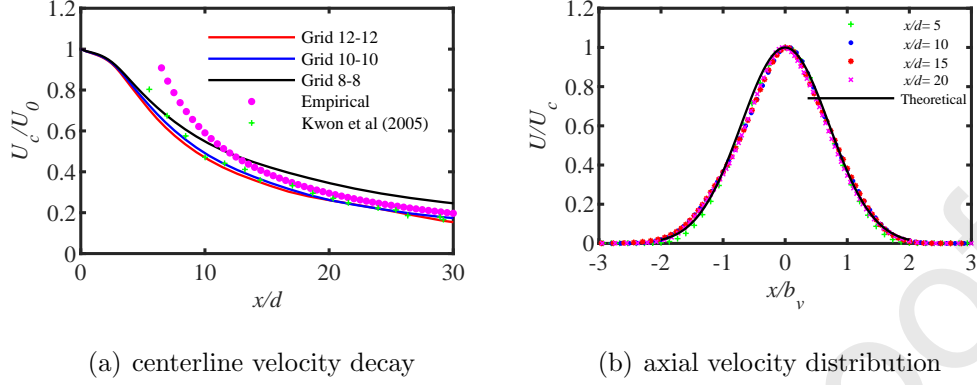


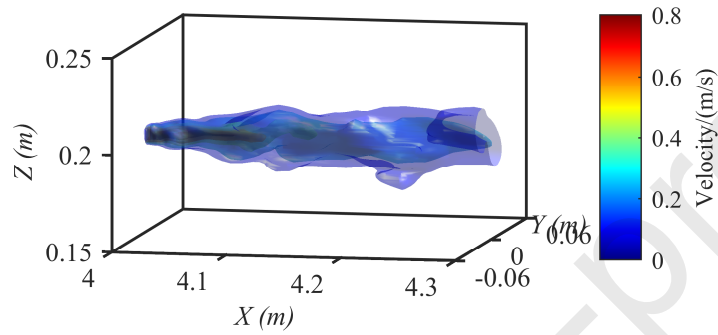
Figure 12: Comparison of (a) centerline velocity decay with different grids; (b) axial velocity distribution (b_v means jet Gaussian half-width) between experiments and numerical simulation.

528 different kinds of particle diameters are used in the simulation. Particles were
 529 put into different grid cells on the jet outlet boundary. A Gaussian white
 530 noise is applied to determine the precise time step for particle release from the
 531 jet boundary as particles do not exit each grid cell at every time step. This
 532 initial artificial asymmetry in particle distribution can be quickly dissipated
 533 by turbulence as the jet flow develops downstream, having minimal impact
 534 on the final results [75].

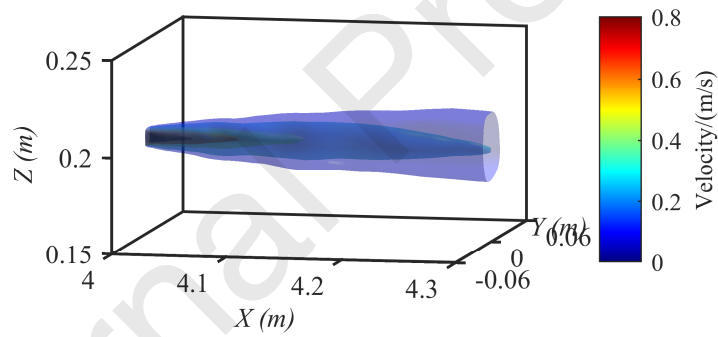
535 The 1-D deposition pattern is shown in Figure 14(b). To ensure the
 536 repeatability and avoid the effect of noise in particle numbers on the final
 537 deposition pattern, two different particle numbers namely 81000 and 162000
 538 particles are adopted in the numerical simulation. It can be seen from the
 539 figure that the simulated 1-D deposition pattern matches well with the ex-
 540 periments. The deposition pattern shares great similarity when using 81000
 541 or 162000 particles. Therefore, the number of sediment particles is set to
 542 81000 hereafter to reduce computational cost.

543 The two-dimensional deposition pattern is shown in Figure 15. The black
 544 contour lines are the 2-D deposition concentration which equals the deposi-
 545 tion rate divided by the bottom grid size. The profiles are consistent with the
 546 previously measured 1-D deposition profiles, with a peak deposition at about
 547 0.2 m from the jet orifice for this case. It can also be seen that the sediment
 548 deposition would expand, and deposition patterns are almost symmetric.

549 Figure 16 shows the three-dimensional visualization of a horizontal sediment-



(a) Instantaneous velocity isosurface



(b) Time-averaged velocity isosurface

Figure 13: Comparison of (a) instantaneous and (b) time-averaged velocity isosurfaces of the jet in a stationary environment, with isosurfaces shown at velocity magnitudes of 0.2 m/s to 0.8 m/s, in 0.2 m/s increments.

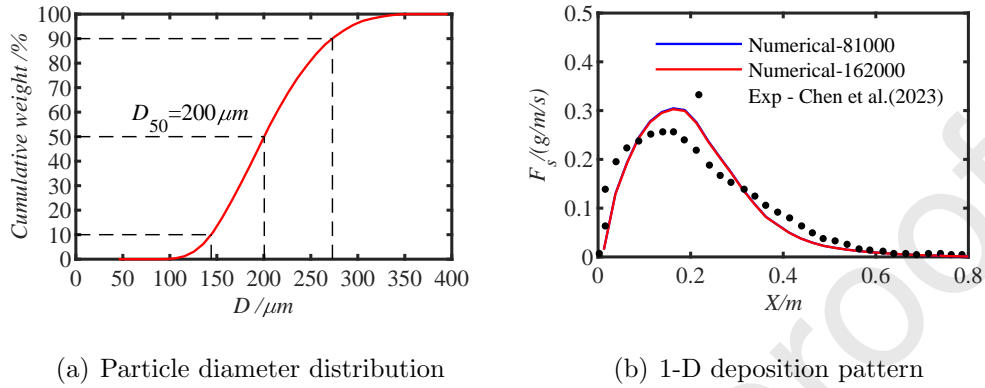


Figure 14: Verification of sediment-laden jet in an initially stationary environment, (a) particle diameter distribution; (b) 1-D deposition pattern.

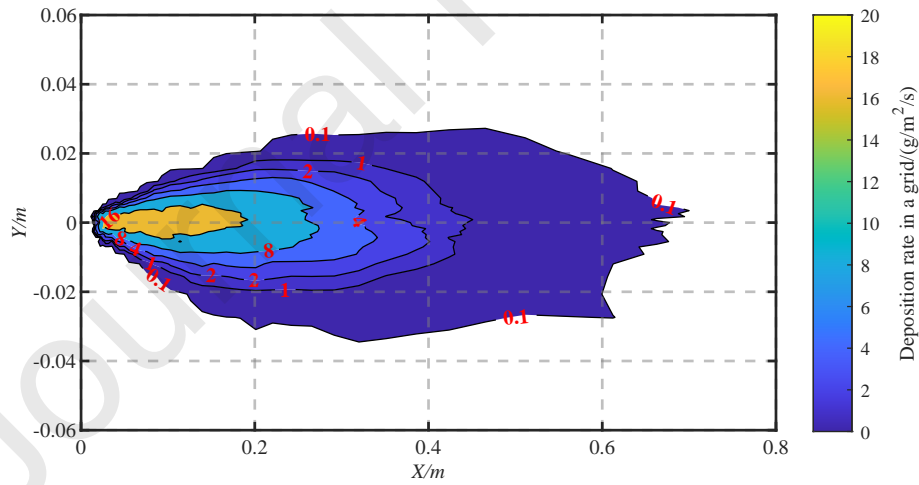


Figure 15: 2-D deposition pattern of sediment-laden jet in an initially stationary environment (Top View).

550 laden jet in in a stationary environment. The positions of the sediment
 551 particles are marked as spheres, while their instantaneous velocities are dis-
 552 tinguished by various colours. The visualization clearly shows that sediments
 553 initially follow the flow movement in the near field. As the flow velocity de-
 554 creases downstream, the sediments would gradually deviate from the jet cen-
 555 terline (i.e., $z = 0.18$ m) and move downward due to gravity. Consequently,
 556 fewer sediments are observed in the upper part of the jet cross-sections (i.e.,
 557 $z > 0.18$ m) and hardly can sediment be seen in the upper part of jet far field
 558 (i.e., $x > 0.6$ m).

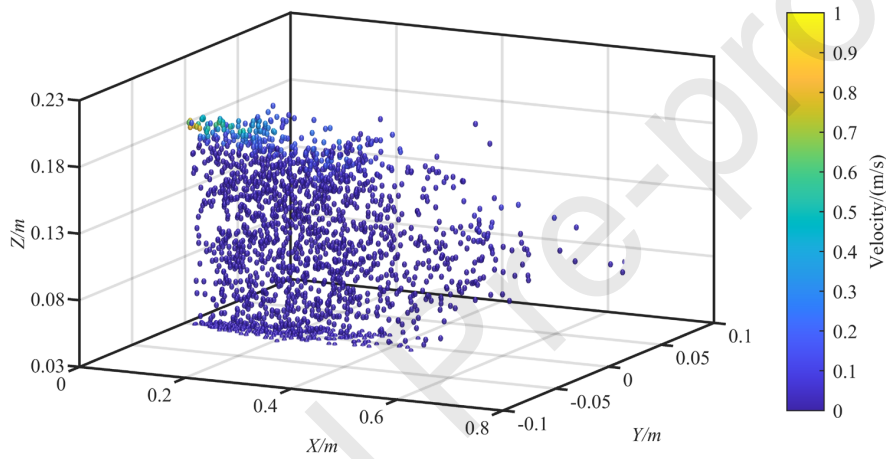


Figure 16: 3-D visualization of sediment-laden jet in an initially stationary environment.

559 4.5. Benchmark: sediment-laden jet in flow with waves

560 Finally, we further use this model to simulate a sediment-laden jet in
 561 flow with waves. The experiments were carried out within a wave flume
 562 located at the College of Harbor, Coastal and Offshore Engineering, Hohai
 563 University. Figure 17 shows a sketch of the experimental setup. The flume
 564 dimensions were 46 m in length, 0.5 m in width, and 1.0 m in depth. All
 565 experiments consisted of four systems, namely the wave generating system,
 566 the sediment-laden jet generating system, the measuring system, and the
 567 collection system. The wave generating system consisted of a wave paddle
 568 and an absorber. This system was used to make regular waves. The sediment-
 569 laden jet generating system mainly consisted of a constant head tank which
 570 was full of feeding particles and settling equipment to feed sediment into

571 the flow. The measuring system consisted of a continuous laser machine
 572 and two high-speed cameras, which made it into a PIV system. Finally, the
 573 collection tray was used to collect all the settled sediment. A horizontal
 574 jet was introduced through an acrylic nozzle with a diameter of 0.01 m.
 575 The nozzle was positioned at the flume's midpoint, maintaining a 0.18 m
 576 clearance above the bottom. To maintain a consistent exit velocity, water
 577 was continuously pumped at a constant head, while the discharge rate was
 578 controlled by a rotameter. The wave height was 0.022 m and the wave period
 579 was set as 1.5 s. To fix the jet position in flow with waves, a double-layer
 580 σ coordinate [76] is adopted in the simulation. The computational domain
 581 is 15 m in length, 0.5 m in width, 0.5 m in depth and is discretized by
 582 $368 \times 41 \times 139$ grids. A non-uniform grid is employed and refined at the jet
 583 orifice, with minimum grid sizes in the x , y , and σ directions of 0.1 m. The
 584 time step is set to 0.002 s and the total CPU time per time step required
 585 for the present model was about 10.2 s. The jet outlet velocity is set as 0.85
 586 m/s. As it was found in the former section the number of sediment particles
 587 has no impact on the final deposition outcome once it exceeds 81000, the
 588 number of particles is set to be 81000 and these particles are injected at each
 589 grid on the jet outflow boundary.

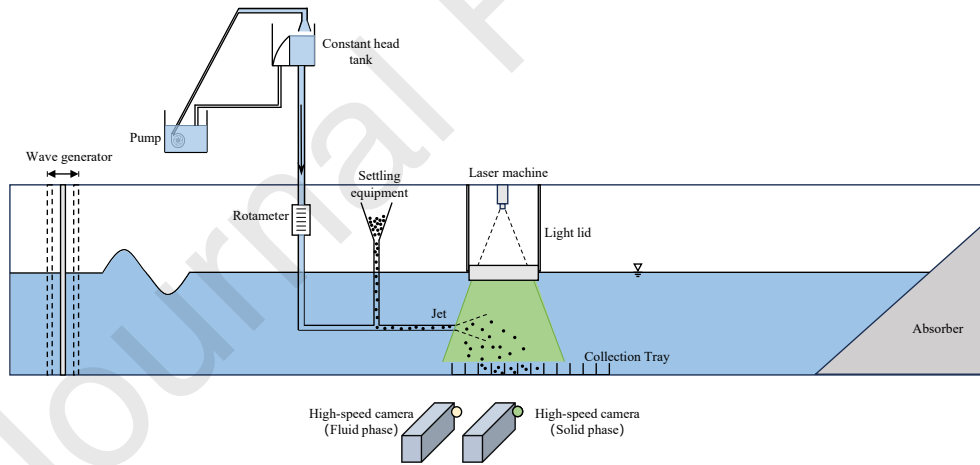


Figure 17: Experimental set up.

590 Figure 18(a) shows the comparison of the velocity distribution of hori-
 591 zontal jet under wave conditions between experimental data and numerical
 592 results at $x/d = 15$ and $x/d = 30$. It suggests that the simulated velocity

593 profiles have the same trend as that in the experiments but the values are
 594 over-predicted. The main reason for this outcome is that, in the experiments,
 595 the elevation inside the sediment-feeding system would change in accordance
 596 with the outside elevation changes due to the existence of waves. As a result,
 597 the outflow velocity near the jet orifice varies within a wave cycle. Therefore,
 598 an extra oscillation velocity should be added to the jet outlet velocity. How-
 599 ever, this simulation does not consider such specific phenomena. Nonetheless,
 600 the velocity remains consistent with the experimental data.

601 Figure 18(b) shows the 1-D deposition pattern of the horizontal sediment-
 602 laden jet in flow with waves and initially stationary water. The results indi-
 603 cate that the simulated deposition aligns closely with experimental data,
 604 except in the relatively far field where increased sediment deposition is ob-
 605 served when compared to that in the experiments. This discrepancy may be
 606 due to the comparatively high outflow velocity used in our simulation. In
 607 addition, compared with the sediment-laden jet in initially stationary water,
 608 it is found that the deposition rate decreases in the near field while a higher
 609 deposition rate is observed in the middle and far-field when the sediment-
 610 laden jet is injected under wavy conditions, which are well captured by the
 611 model.

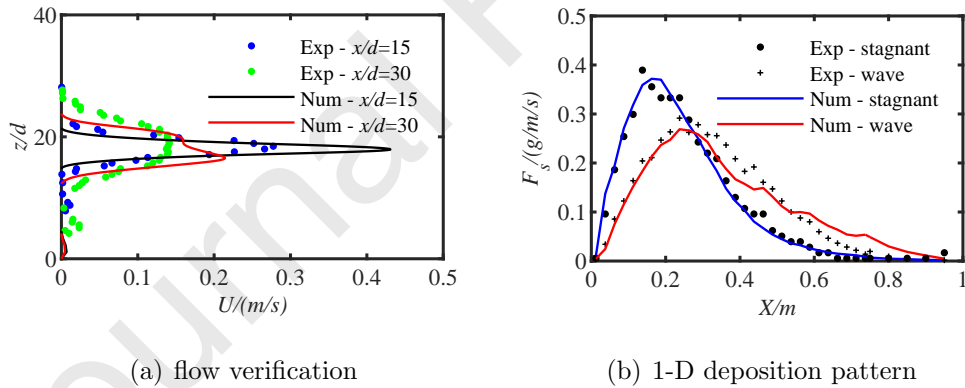


Figure 18: Comparison of the numerical model and the experimental results of sediment-laden jet in flow with waves, (a) flow field; (b) 1-D deposition pattern.

612 The comparison of instantaneous sediment distribution between the nu-
 613 merical model and the experimental results of the sediment-laden jet at wave
 614 peak phase is shown in Figure 19. Figure 19(a) shows the original experi-
 615 mental image, while Figure 19(b) presents the same image with an inverted

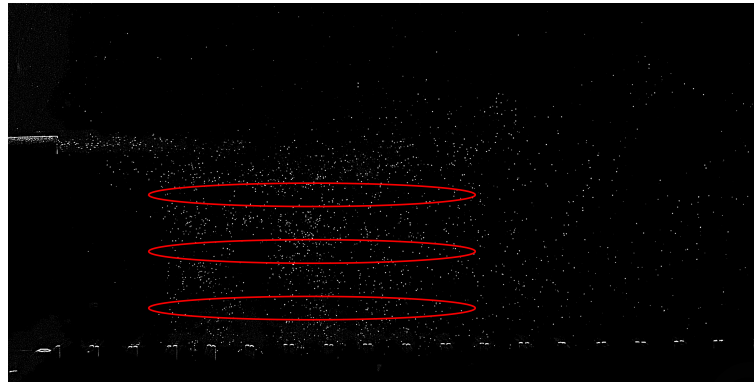
616 grayscale for better comparison with numerical simulation results. Obvious
617 discontinuities in sediment deposition which are marked in red ellipses can be
618 seen in Figure 19(b). The discontinuities also show periodic changes, which
619 are likely to be attributed to the impact of the wave. The numerical results
620 capture the overall pattern well. In positions closer to the bottom, discontinuities
621 remain clearly visible in our model, whereas they are hardly to be
622 observed in the experiments. The main reason is that the sediment particles
623 adopted in our model are chosen to have the same diameter, which is different
624 from the experiments. Consequently, once the particles leave the jet body,
625 they tend to move at the same speed due to uniform settling velocities. As a
626 result, discontinuities remain clearly visible in our model even in areas close
627 to the bottom.

628 A set of three-dimensional visualizations of the horizontal sediment-laden
629 jet at different wave phases are shown in Figure 20. It can be seen that particles
630 would sway upward and downward under wave conditions, which is the
631 most distinctive deposition pattern compared to the initially stationary case.
632 Additionally, the visualizations also reveal that particles are transported further
633 under the effect of waves. Figure 21 shows the two-dimensional (2-D)
634 deposition pattern of the sediment-laden jet under wave conditions. The 2-D
635 sediment concentration contour lines cover a confined area with higher deposition
636 rates, specifically when the deposition rate in a grid is larger than $16 \text{ g/m}^2/\text{s}$;
637 whereas they cover a broader area in smaller values like when the deposition
638 rate in a grid is less than $1 \text{ g/m}^2/\text{s}$. In summary, the model captures
639 the behavior of the horizontal sediment-laden jet under wave conditions.

640 5. Conclusion

641 This paper introduces a two-phase flow model that couples the non-
642 hydrostatic model with the point-particle model to simulate sediment-laden
643 flow problems associated with temporal changes in the free surface. A Lagrangian-
644 Eulerian method is utilized to track the free surface, and the movement of
645 sediment particles is tracked by a point-particle model. The model's accuracy
646 is validated through comparison with five distinct cases.

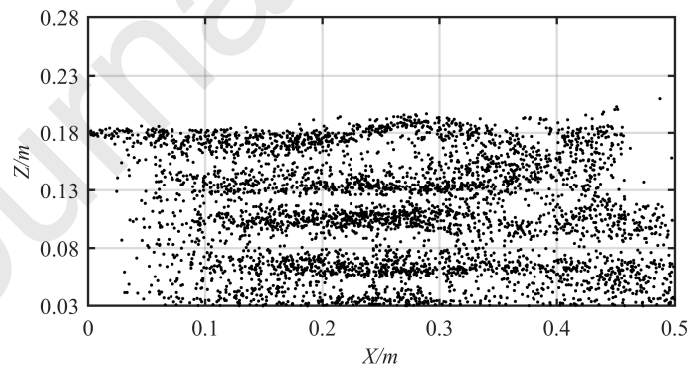
647 First, the propagation of regular waves at a constant depth is simulated
648 using this model. It is found that both the free surface and flow fields match
649 well with analytical solutions. The model is then extended to address varying
650 water depth scenarios, specifically the interaction of regular waves with a
651 submerged bar. The numerical results also correspond well with experimental



(a) Experiment - original image

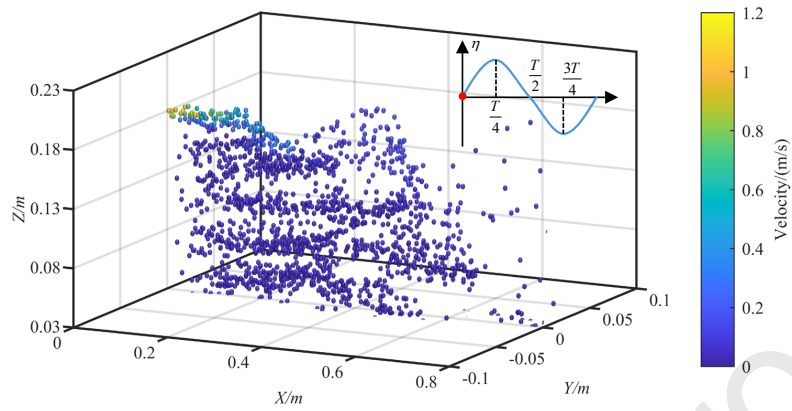


(b) Experiment - invert the grayscale of the original image

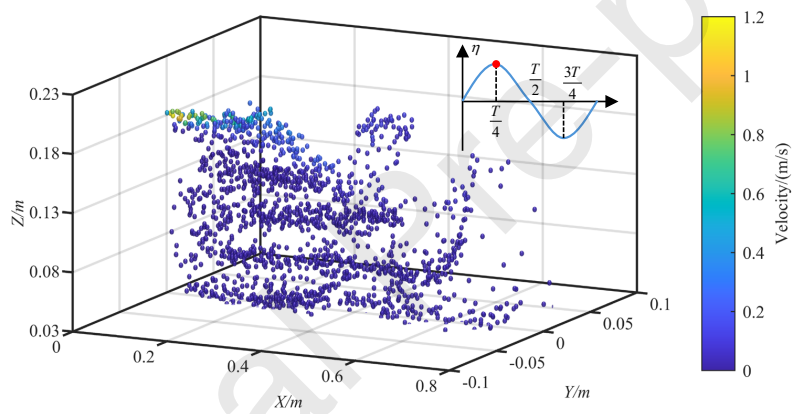


(c) Numerical

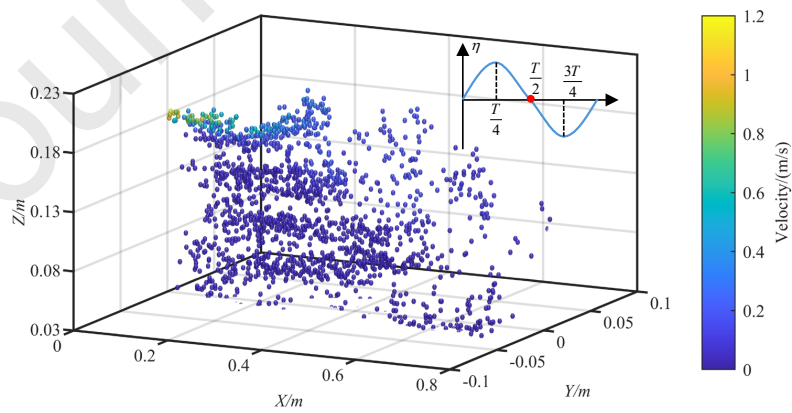
Figure 19: Comparison of instantaneous sediment distribution between the numerical model and the experimental results of sediment-laden jet at wave peak phase.



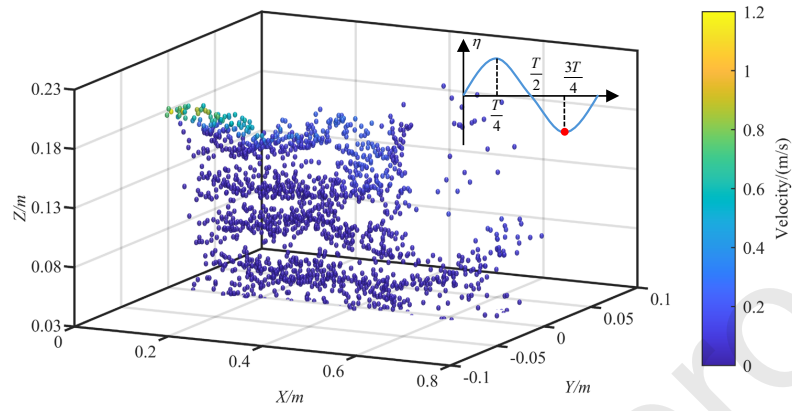
(a) Wave up-crossing



(b) Wave peak



(c) Wave down-crossing



(d) Wave trough

Figure 20: 3-D visualization of initial stage of sediment-laden jet in flow with waves at four different wave phases (a) Wave up-crossing, (b) Wave peak, (c) Wave down-crossing and (d) Wave trough.

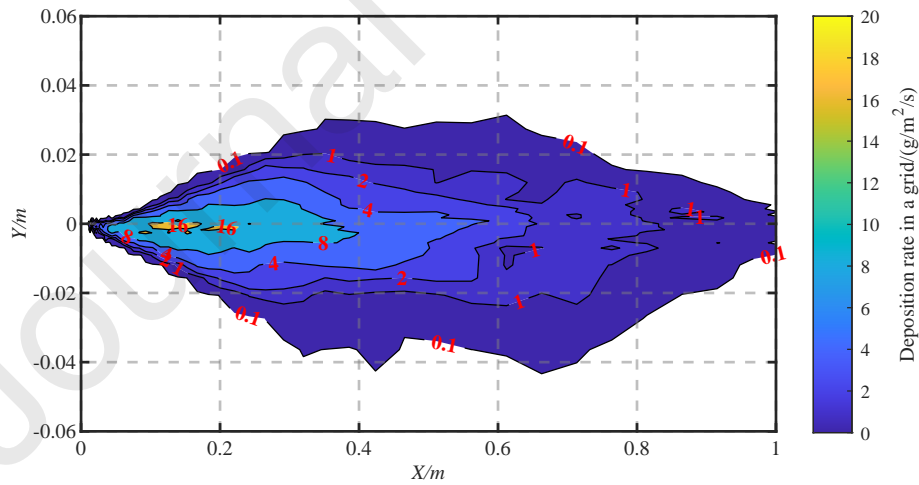


Figure 21: 2-D deposition pattern of sediment-laden jet in flow with waves.

652 findings. This underscores the model's effectiveness in simulating behaviour
653 related to changes in free surface. After that, the verification of the point-
654 particle model is conducted. The deposition processes of a single particle,
655 both in stationary and oscillating environments are simulated, yielding re-
656 sults that closely match with analytical solutions and experimental data.
657 Finally, the two-phase flow model, integrated with the point-particle model,
658 is employed to simulate a dilute horizontal sediment-laden jet in both sta-
659 tionary and wave environments. The observed deposition patterns are found
660 to be in line with experimental outcomes, affirming the model's capability to
661 accurately represent sediment transport processes.

662 The new model shows significant potential as a numerical tool for simu-
663 lating sediment-laden free surface flows. Currently, the point-particle model
664 is limited to one-way coupling with the flow, where the reaction force of
665 particles on the flow and the collisions between particles are not considered.
666 This limitation makes it primarily suitable for low-concentration sediment-
667 laden flows. In the future, the reaction force of particles on the flow will be
668 incorporated into the governing equation as a source term, and either the
669 soft-sphere [77] model or hard-sphere model [78] will be employed for the
670 dispersed phase to simulate problems with higher sediment concentrations.

671 Acknowledgments

672 This work was supported by the National Key Research and Development
673 Program of China (2023YFC3008100), the National Natural Science Founda-
674 tion of China (51979076, 52211530103) and United Kingdom Engineering and
675 Physical Sciences Research Council (EPSRC) grant (EP/V040235/1). The
676 first author also would like to acknowledge the financial support from the
677 China Scholarship Council (CSC) under PhD exchange program at Cardiff
678 University [202206710100]. Constructive comments from anonymous review-
679 ers have helped to improve the manuscript and these are gratefully acknowl-
680 edged. Special thanks are also given to editors for their meticulous handling
681 of the manuscript and dedication throughout the review process, which has
682 significantly enhanced the readability and overall quality of this work.

683 References

- 684 [1] D. J. Piper, P. Cochonat, M. L. Morrison, The sequence of events around
685 the epicentre of the 1929 grand banks earthquake: initiation of debris

- 686 flows and turbidity current inferred from sidescan sonar, *Sedimentology*
687 46 (1999) 79–97.
- 688 [2] J. Syvitski, J. R. Ángel, Y. Saito, I. Overeem, C. J. Vörösmarty,
689 H. Wang, D. Olago, Earth’s sediment cycle during the anthropocene,
690 *Nat. Rev. Earth Environ.* 3 (2022) 179–196.
- 691 [3] J. L. Li, G. X. Wang, C. L. Song, S. Q. Sun, J. P. Ma, Y. Wang,
692 L. M. Guo, D. F. Li, Recent intensified erosion and massive sediment
693 deposition in tibetan plateau rivers, *Nat. Commun.* 15 (2024) 722.
- 694 [4] J. K. Reece, R. M. Dorrell, K. M. Straub, Circulation of hydraulically
695 ponded turbidity currents and the filling of continental slope minibasins,
696 *Nat. Commun.* 15 (2024) 2075.
- 697 [5] E. Stokstad, Prospect of unregulated deep-sea mining looms, *Science*
698 381 (2023) 254–255.
- 699 [6] P. J. Talling, S. Hage, M. L. Baker, T. S. Bianchi, R. G. Hilton, K. L.
700 Maier, The global turbidity current pump and its implications for or-
701 ganic carbon cycling, *Annu. Rev. Mar. Sci.* 16 (2024) 105–133.
- 702 [7] P. Dong, K. F. Zhang, Two-phase flow modelling of sediment motions
703 in oscillatory sheet flow, *Coast. Eng.* 36 (1999) 87–109.
- 704 [8] T.-J. Hsu, J. T. Jenkins, P. L.-F. Liu, On two-phase sediment transport:
705 sheet flow of massive particles, *Proceedings of the Royal Society of*
706 *London. Series A: Mathematical, Physical and Engineering Sciences* 460
707 (2004) 2223–2250.
- 708 [9] L. Amoudry, T.-J. Hsu, P.-F. Liu, Two-phase model for sand transport
709 in sheet flow regime, *J. Geophys. Res. Oceans* 113 (2008).
- 710 [10] T. Revil-Baudard, J. Chauchat, A two-phase model for sheet flow regime
711 based on dense granular flow rheology, *J. Geophys. Res. Oceans* 118
712 (2013) 619–634.
- 713 [11] Z. Cheng, T.-J. Hsu, J. Calantoni, Sedfoam: A multi-dimensional Eu-
714 lerian two-phase model for sediment transport and its application to
715 momentary bed failure, *Coast. Eng.* 119 (2017) 32–50.

- 716 [12] A. Mathieu, Z. Cheng, J. Chauchat, C. Bonamy, T.-J. Hsu, Numerical
717 investigation of unsteady effects in oscillatory sheet flows, *J. Fluid Mech.*
718 943 (2022) A7.
- 719 [13] I. Vinkovic, D. Doppler, J. Lelouvetel, M. Buffat, Direct numerical
720 simulation of particle interaction with ejections in turbulent channel
721 flows, *Int. J. Multiphase Flow* 37 (2011) 187–197.
- 722 [14] R. Sun, H. Xiao, CFD-DEM simulations of current-induced dune for-
723 mation and morphological evolution, *Adv. Water Resour.* 92 (2016)
724 228–239.
- 725 [15] D. Wildt, C. Hauer, H. Habersack, M. Tritthart, LES two-phase mod-
726 elling of suspended sediment transport using a two-way coupled Euler-
727 Lagrange approach, *Adv. Water Resour.* 160 (2022) 104095.
- 728 [16] J. F. Xie, P. Hu, C. L. Zhu, Z. S. Yu, T. Pätz, Turbidity currents
729 propagating down an inclined slope: particle auto-suspension, *J. Fluid*
730 *Mech.* 954 (2023) A44.
- 731 [17] A. Shakibaeinia, Y.-C. Jin, MPS mesh-free particle method for multi-
732 phase flows, *Comput. Method Appl. M.* 229 (2012) 13–26.
- 733 [18] C. Ulrich, M. Leonardi, T. Rung, Multi-physics SPH simulation of
734 complex marine-engineering hydrodynamic problems, *Ocean Eng.* 64
735 (2013) 109–121.
- 736 [19] Q. H. Ran, J. Tong, S. D. Shao, X. D. Fu, Y. P. Xu, Incompressible
737 SPH scour model for movable bed dam break flows, *Adv. Water Resour.*
738 82 (2015) 39–50.
- 739 [20] H. B. Shi, X. P. Yu, R. A. Dalrymple, Development of a two-phase SPH
740 model for sediment laden flows, *Comput. Phys. Commun.* 221 (2017)
741 259–272.
- 742 [21] M. A. Nabian, L. Farhadi, Multiphase mesh-free particle method for
743 simulating granular flows and sediment transport, *J. Hydraul. Eng.* 143
744 (2017) 04016102.
- 745 [22] M. Wang, Y. Pan, X. Shi, J. Wu, P. Sun, Comparative study on volume
746 conservation among various sph models for flows of different levels of
747 violence, *Coastal Engineering* 191 (2024) 104521.

- 748 [23] J. R. Finn, M. Li, S. V. Apte, Particle based modelling and simulation
749 of natural sand dynamics in the wave bottom boundary layer, *J. Fluid*
750 *Mech.* 796 (2016) 340–385.
- 751 [24] M. R. Maxey, J. J. Riley, Equation of motion for a small rigid sphere in
752 a nonuniform flow, *Phys. Fluids* 26 (1983) 883–889.
- 753 [25] C. S. Peskin, Flow patterns around heart valves: a digital computer
754 method for solving the equations of motion, Yeshiva Uni., 1972.
- 755 [26] M. Uhlmann, An immersed boundary method with direct forcing for the
756 simulation of particulate flows, *J. Comput. Phys.* 209 (2005) 448–476.
- 757 [27] A. G. Kidanemariam, M. Uhlmann, Direct numerical simulation of
758 pattern formation in subaqueous sediment, *J. Fluid Mech.* 750 (2014)
759 R2.
- 760 [28] M. Uhlmann, Interface-resolved direct numerical simulation of vertical
761 particulate channel flow in the turbulent regime, *Phys. Fluids* 20 (2008).
- 762 [29] A. Prosperetti, Life and death by boundary conditions, *J. Fluid Mech.*
763 768 (2015) 1–4.
- 764 [30] Z. Jiang, P. Haff, Multiparticle simulation methods applied to the mi-
765 cro-mechanics of bed load transport, *Water Resour. Res.* 29 (1993) 399–
766 412.
- 767 [31] M. A. van der Hoef, M. van Sint Annaland, N. Deen, J. Kuipers, Numer-
768 ical simulation of dense gas-solid fluidized beds: a multiscale modeling
769 strategy, *Annu. Rev. Fluid Mech.* 40 (2008) 47–70.
- 770 [32] S. Apte, K. Mahesh, T. Lundgren, Accounting for finite-size effects in
771 simulations of disperse particle-laden flows, *Int. J. Multiphase Flow* 34
772 (2008) 260–271.
- 773 [33] J. Capecelatro, O. Desjardins, Eulerian–Lagrangian modeling of turbu-
774 lent liquid–solid slurries in horizontal pipes, *Int. J. Multiphase Flow* 55
775 (2013) 64–79.
- 776 [34] A. Hager, C. Kloss, S. Pirker, C. Goniva, Parallel resolved open source
777 CFD-DEM: method, validation and application, *J. Comput. Multiph.*
778 *Flows* 6 (2014) 13–27.

- 779 [35] C. W. Hirt, B. D. Nichols, Volume of Fluid (VOF) method for the
780 dynamics of free boundaries, *J. Comput. Phys.* 39 (1981) 201–225.
- 781 [36] T. Shan, J. D. Zhao, A coupled CFD-DEM analysis of granular flow
782 impacting on a water reservoir, *Acta Mech.* 225 (2014) 2449–2470.
- 783 [37] L. Jing, C. Kwok, Y. F. Leung, Y. Sobral, Extended CFD-DEM for
784 free-surface flow with multi-size granules, *Int. J. Numer. Anal. Methods*
785 *Geomech.* 40 (2016) 62–79.
- 786 [38] Z. H. Shen, G. Wang, D. R. Huang, F. Jin, A resolved CFD-DEM
787 coupling model for modeling two-phase fluids interaction with irregularly
788 shaped particles, *J. Comput. Phys.* 448 (2022) 110695.
- 789 [39] W. X. Li, H. B. Shi, X. P. Yu, A DEM-based Euler–Lagrange model
790 for motion of particle–fluid two-phase mixtures, *Acta Geotech.* (2023)
791 1–19.
- 792 [40] C. F. Ai, Y. X. Ma, C. F. Yuan, G. H. Dong, A 3D non-hydrostatic
793 model for wave interactions with structures using immersed boundary
794 method, *Comput. Fluids* 186 (2019) 24–37.
- 795 [41] P. Z. Lin, C. W. Li, A σ -coordinate three-dimensional numerical model
796 for surface wave propagation, *Int. J. Numer. Methods Fluids* 38 (2002)
797 1045–1068.
- 798 [42] G. F. Ma, F. Y. Shi, J. T. Kirby, Shock-capturing non-hydrostatic model
799 for fully dispersive surface wave processes, *Ocean Model.* 43 (2012) 22–
800 35.
- 801 [43] M. Zijlema, G. S. Stelling, Further experiences with computing non-
802 hydrostatic free-surface flows involving water waves, *Int. J. Numer.*
803 *Methods Fluids* 48 (2005) 169–197.
- 804 [44] M. Zijlema, G. Stelling, Efficient computation of surf zone waves using
805 the nonlinear shallow water equations with non-hydrostatic pressure,
806 *Coast. Eng.* 55 (2008) 780–790.
- 807 [45] C. F. Ai, S. Jin, B. Lv, A new fully non-hydrostatic 3D free surface flow
808 model for water wave motions, *Int. J. Numer. Methods Fluids* 66 (2011)
809 1354–1370.

- 810 [46] Y. P. Chen, C. W. Li, C. K. Zhang, Numerical modeling of a round jet
811 discharged into random waves, *Ocean Eng.* 35 (2008) 77–89.
- 812 [47] Z. S. Xu, Y. P. Chen, J. F. Tao, Y. Pan, D. M. Sowa, C. W. Li, Three-
813 dimensional flow structure of a non-buoyant jet in a wave-current coex-
814 isting environment, *Ocean Eng.* 116 (2016) 42–54.
- 815 [48] Z. S. Xu, Y. P. Chen, Y. N. Wang, C. K. Zhang, Near-field dilution of
816 a turbulent jet discharged into coastal waters: Effect of regular waves,
817 *Ocean Eng.* 140 (2017) 29–42.
- 818 [49] Z. S. Xu, Y. P. Chen, Y. Pan, Initial dilution equations for wastew-
819 ater discharge: Example of non-buoyant jet in wave-following-current
820 environment, *Ocean Eng.* 164 (2018) 139–147.
- 821 [50] G. Ma, J. T. Kirby, F. Shi, Numerical simulation of tsunami waves
822 generated by deformable submarine landslides, *Ocean Model.* 69 (2013)
823 146–165.
- 824 [51] N. A. Berard, R. P. Mulligan, A. M. F. da Silva, M. Dibajnia, Evaluation
825 of XBeach performance for the erosion of a laboratory sand dune, *Coast.*
826 *Eng.* 125 (2017) 70–80.
- 827 [52] C. Zhang, J. T. Kirby, F. Y. Shi, G. F. Ma, S. T. Grilli, A two-
828 layer non-hydrostatic landslide model for tsunami generation on irregu-
829 lar bathymetry. 2. numerical discretization and model validation, *Ocean*
830 *Model.* 160 (2021) 101769.
- 831 [53] J. Smagorinsky, General circulation experiments with the primitive
832 equations: I. the basic experiment, *Mon. Weather Rev.* 91 (1963) 99–
833 164.
- 834 [54] P. Lin, *Numerical modeling of water waves*, CRC Press, 2008.
- 835 [55] P. Z. Lin, P. L.-F. Liu, A numerical study of breaking waves in the surf
836 zone, *J. Fluid Mech.* 359 (1998) 239–264.
- 837 [56] J. Mani, S. Jayakumar, Wave transmission by suspended pipe break-
838 water, *Journal of waterway, port, coastal, and ocean engineering* 121
839 (1995) 335–338.

- 840 [57] S. Neelamani, R. Rajendran, Wave interaction with t-type breakwaters,
841 Ocean Engineering 29 (2002) 151–175.
- 842 [58] X. Yu, Diffraction of water waves by porous breakwaters, Journal of
843 waterway, port, coastal, and ocean engineering 121 (1995) 275–282.
- 844 [59] J. C. Park, M. H. Kim, H. Miyata, Fully non-linear free-surface simu-
845 lations by a 3D viscous numerical wave tank, Int. J. Numer. Methods
846 Fluids 29 (1999) 685–703.
- 847 [60] N. Jarrin, S. Benhamadouche, D. Laurence, R. Prosser, A synthetic-
848 eddy-method for generating inflow conditions for large-eddy simulations,
849 Int. J. Heat Fluid Flow 27 (2006) 585–593.
- 850 [61] Z. M. Lu, M. Z. Yuan, The LDA measurement of turbulent flow in
851 square duct and the comparison of some flow characteristics with pipe
852 flow, Acta Mech. Sinica 18 (1986).
- 853 [62] X. H. Wu, P. Moin, A direct numerical simulation study on the mean
854 velocity characteristics in turbulent pipe flow, J. Fluid Mech. 608 (2008)
855 81–112.
- 856 [63] C. W. Li, T. Yu, Numerical investigation of turbulent shallow recircu-
857 lating flows by a quasi-three-dimensional $k - \epsilon$ model, Int. J. Numer.
858 Methods Fluids 23 (1996) 485–501.
- 859 [64] N. N. Janenko, The method of fractional steps, volume 160, Springer,
860 1971.
- 861 [65] L. Zhu, C. W. Li, Error study on numerical approximation of radia-
862 tion boundary condition for one-dimensional wave equation, Commun.
863 Numer. Methods Eng. 9 (1993) 475–482.
- 864 [66] Y. P. Chen, C. W. Li, C. K. Zhang, Development of a fully nonlinear
865 numerical wave tank, China Ocean Eng. 18 (2004) 501–514.
- 866 [67] S. N. Chan, Mixing and deposition of sediment-laden buoyant jets, HKU
867 Theses Online (HKUTO) (2013).
- 868 [68] S. Beji, J. Battjes, Experimental investigation of wave propagation over
869 a bar, Coast. Eng. 19 (1993) 151–162.

- 870 [69] L. M. Brush Jr, H.-W. Ho, B.-C. Yen, Accelerated motion of a sphere
871 in a viscous fluid, *J. Hydr. Eng. Div.* 90 (1964) 149–160.
- 872 [70] N. Mordant, J.-F. Pinton, Velocity measurement of a settling sphere,
873 *Eur. Phys. J. B* 18 (2000) 343–352.
- 874 [71] H.-W. Ho, Fall velocity of a sphere in a field of oscillating fluid, The
875 Uni. of Iowa, 1964.
- 876 [72] Y. P. Chen, E. Otoo, Y. H. Chen, Z. S. Xu, X. F. Li, Y. Zhou, Deposition
877 behaviour of inclined momentum sediment-laden jet, *Ocean Eng.* 278
878 (2023) 114399.
- 879 [73] L. Brandt, F. Coletti, Particle-laden turbulence: progress and perspec-
880 tives, *Annu. Rev. Fluid Mech.* 54 (2022) 159–189.
- 881 [74] S. J. Kwon, I. W. Seo, Reynolds number effects on the behavior of a
882 non-buoyant round jet, *Exp. Fluids* 38 (2005) 801–812.
- 883 [75] P. Liu, K. M. Lam, Large-eddy simulation of horizontally discharging
884 sediment-laden jets, *Journal of Hydro-environment Research* 9 (2015)
885 388–403.
- 886 [76] Y. Chen, Y. Chen, Z. Xu, P. Lin, Z. Xie, A double-layer non-hydrostatic
887 model for simulating wave-structure and wave-jet interactions, *Journal*
888 *of Computational Physics* 523 (2025) 113634.
- 889 [77] P. A. Cundall, O. D. Strack, A discrete numerical model for granular
890 assemblies, *Geotechnique* 29 (1979) 47–65.
- 891 [78] H. P. Zhu, Z. Y. Zhou, R. Yang, A. Yu, Discrete particle simulation
892 of particulate systems: theoretical developments, *Chemical Engineering*
893 *Science* 62 (2007) 3378–3396.

Declaration of interests

The authors declare that they have no known competing financial interests or personal relationships that could have appeared to influence the work reported in this paper.

The authors declare the following financial interests/personal relationships which may be considered as potential competing interests:

Journal Pre-proof